

# CoMo3R-SLAM: Collaborative Monocular Dense SLAM with Learned 3D Reconstruction Priors for Outdoor Multi-Agent Systems

Zhihao Cao<sup>1</sup> Qi Shao<sup>2,3</sup> Shuhao Zhai<sup>4</sup> Feng Tian<sup>1</sup>

Anh Nguyen<sup>2</sup> Hesheng Wang<sup>5</sup> Baoru Huang<sup>2,6</sup>

<sup>1</sup>ETH Zurich <sup>2</sup>University of Liverpool <sup>3</sup>Harbin Engineering University

<sup>4</sup>University of Ottawa <sup>5</sup>Shanghai Jiao Tong University <sup>6</sup>Imperial College London

**Abstract:** Collaborative dense SLAM is essential for multi-robot teams to achieve scalable and consistent 3D perception across large-scale outdoor environments. Existing systems typically depend on depth sensors, incurring significant payload, power, and calibration costs. Monocular RGB cameras are a lightweight alternative, but collaborative monocular dense SLAM remains difficult due to scale ambiguity, unreliable inter-agent data association, especially in outdoor scenes where low overlap and repetitive structures make traditional feature matching unreliable, motivating robust geometric information. We propose CoMo3R-SLAM, the first collaborative monocular dense RGB SLAM system that leverages robust learned feed-forward 3D reconstruction priors for outdoor multi-agent mapping. Each agent runs a prior-guided front-end for real-time tracking and local dense fusion, while a coordinator performs dense pointmap matching for cross-agent verification, closed-form Sim(3) gauge synchronization, and GPU-accelerated global bundle adjustment with segment-level depth optimization. Requiring neither depth sensors nor parametric intrinsics, our system produces robust cross-agent constraints and globally consistent metric maps from monocular RGB alone. On Tanks and Temples (T&T) and Waymo sequences, CoMo3R-SLAM achieves the best ATE on three of four T&T scenes and competitive Waymo accuracy, matching or exceeding state-of-the-art RGB-D methods while running online at 8 FPS.

**Keywords:** Multi-agent Systems, Dense SLAM, Learning-based 3D Priors

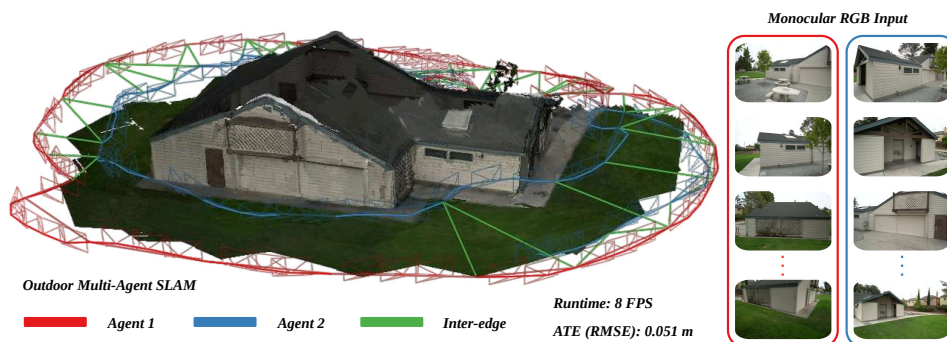


Figure 1: CoMo3R-SLAM performs collaborative monocular dense SLAM from two RGB-only agent streams on the outdoor Barn scene [1]. Given monocular image sequences with limited cross-agent overlap, our system estimates globally aligned camera trajectories, establishes inter-agent constraints, and reconstructs a consistent dense scene geometry without depth sensors, running at 8 FPS with an ATE RMSE of 0.051 m. The anonymous project website of CoMo3R-SLAM is available at <https://como3r-slam.github.io>.

# 1 Introduction

Outdoor multi-robot teams deployed in search and rescue, environmental monitoring, and cooperative autonomous driving must construct and maintain a shared, globally consistent 3D understanding of large-scale outdoor environments. Collaborative SLAM addresses this requirement by fusing observations from multiple agents into a single coherent map, enabling robot teams to cover space faster and with greater robustness than any single platform operating in isolation [2, 3].

Most existing collaborative dense SLAM systems achieve metric consistency by relying on active depth sensors [4, 5, 6, 7, 8, 9, 10]. While depth measurements simplify cross-agent alignment to rigid  $SE(3)$  registration, they impose prohibitive payload, power, and calibration overhead for lightweight outdoor robot teams. Monocular RGB cameras therefore constitute an attractive alternative, yet outdoor collaborative monocular dense SLAM remains largely unsolved. Due to monocular scale ambiguity, each agent reconstructs its local map only up to an unknown similarity transform, so inter-agent fusion must estimate both relative pose and scale across independently reconstructed maps. This makes cross-agent alignment highly dependent on reliable visual association, which is particularly challenging outdoors. Existing monocular multi-agent SLAM systems are mainly evaluated in sparse mapping regimes [11, 12] or indoor environments [12, 13, 14], leaving outdoor dense reconstruction underexplored. In large-scale outdoor scenes, low inter-agent overlap, wide view-point changes, complex illumination, and repetitive or textureless structures often make traditional cross-agent feature matching unreliable, preventing robust relative  $Sim(3)$  estimation.

Recent learned feed-forward 3D vision models such as DUS<sub>t</sub>3R [15], MAS<sub>t</sub>3R [16], and VGGT [17] regress dense pointmaps and pixel-level correspondences directly from raw RGB images without known intrinsics or hand-crafted features. These learned priors have already enabled monocular dense SLAM systems [18, 19], that produce globally consistent trajectories and maps. However, all such systems still assume a single continuous trajectory evolving under one gauge. Extending them to multi-agent operation requires (i) detecting shared regions across independent robots, (ii) reconciling per-agent scales, and (iii) fusing partial reconstructions into a common reference frame. We observe that the learning-based priors themselves supply the missing evidence: their metric pointmaps provide a soft scale anchor across agents, while dense, geometry-grounded correspondences enable 3D structural verification more robust than sparse features under outdoor challenges.

Building on this observation, we propose **CoMo3R-SLAM**, the first collaborative monocular dense SLAM framework that places learned 3D reconstruction priors at the center of outdoor multi-agent system. The system follows a two-level hierarchical architecture. Each agent runs a prior-guided front-end that tracks pose and fuses a local dense map from its RGB stream using ray-range residuals on a generic central-camera model. A central coordinator then proposes candidate cross-agent links via retrieval over the prior’s encoder features, verifies them with dense symmetric pointmap matching under a geometric match-fraction test, synchronizes the agents’ independent gauges through a closed-form  $Sim(3)$  alignment, and jointly refines all keyframes via GPU-accelerated global bundle adjustment over a unified multi-agent factor graph with segment-level depth refinement. All tracking and optimization operate in  $Sim(3)$  and assume only a unique camera center, making the system immediately deployable on heterogeneous robot teams with arbitrary, uncalibrated cameras. On challenging outdoor multi-agent benchmarks, CoMo3R-SLAM achieves camera-pose accuracy and globally consistent dense geometry competitive with state-of-the-art RGB-D collaborative methods.

Our main contributions are as follows:

1. We propose CoMo3R-SLAM, the first collaborative monocular dense SLAM framework that systematically incorporates learned feed-forward 3D reconstruction priors at the center of outdoor multi-agent system. A two-level hierarchical architecture couples a prior-guided per-agent front-end with a central coordinator, replacing sparse feature matching with dense learned geometry for both intra- and inter-agent data association.
2. We introduce a prior-guided cross-agent association pipeline that generates candidate links by retrieval over the learning-based prior’s features, verifies them via dense symmetric pointmap

matching under a geometric match-fraction test, and resolves independent agent gauges through closed-form  $\text{Sim}(3)$  alignment, yielding reliable constraints even under low overlap, large viewpoint change, and repetitive outdoor structure.

3. We develop a GPU-accelerated global  $\text{Sim}(3)$  bundle adjustment over a unified multi-agent factor graph constructed from intra- and inter-agent associations with ray-based residuals. The solver is stabilized on ill-conditioned Hessians by a robustified sparse Cholesky factorization and complemented by segment-level depth refinement that alternates pose and depth optimization, all under a generic camera model that assumes only a unique camera center.

## 2 Related Work

### 2.1 Multi-Agent Collaborative Visual SLAM

Collaborative SLAM enables multi-robot teams to jointly localize and map environments beyond any single platform’s reach, which is critical for large-scale outdoor tasks such as search and rescue and cooperative driving. Traditional systems [11, 2, 3, 20, 21] follow the classical pipeline of per-agent tracking, appearance-based place recognition, inter-agent loop closure, and pose-graph optimization, relying almost exclusively on sparse visual features for cross-agent constraints. While effective in well-textured or controlled settings, these sparse associations degrade severely under the low overlap, large viewpoint changes, and repetitive structures common outdoors. Recent dense collaborative methods leverage neural radiance fields [6, 5, 9] and 3D Gaussian Splatting [4, 7, 10, 8, 22, 23] to produce high-fidelity, renderable maps through cross-agent submap fusion. However, they almost universally require RGB-D input, incurring prohibitive payload, power, and calibration costs for lightweight outdoor fleets. Meanwhile, purely monocular collaborative SLAM remains limited to sparse mapping [11, 12], indoor scenarios [12, 13, 14], conventional feature-based inter-agent verification [11, 24], or offline merging [13]. Online outdoor multi-agent dense SLAM from monocular RGB alone thus remains largely unexplored.

### 2.2 Dense Monocular SLAM and Neural Mapping

Classical monocular SLAM has evolved from filtering-based methods such as MonoSLAM [25] to feature-based systems like ORB-SLAM3 [26] and direct methods including LSD-SLAM [27] and DSO [28]. These approaches yield good accuracy given sufficient texture and parallax but produce only sparse or semi-dense maps and require fixed, calibrated intrinsics. Dense monocular SLAM seeks per-pixel geometry: early systems such as DTAM [29] used hand-crafted regularization, while learning-based methods like DROID-SLAM [30] and DPV-SLAM [31] couple learned correspondences with dense bundle adjustment. A parallel line exploits differentiable rendering via neural radiance fields [32, 33, 34, 35, 36, 37, 38] or 3D Gaussian Splatting [39, 40, 41, 42, 43, 44, 45, 46, 47], though most target RGB-D input and assume known parametric intrinsics. Despite strong single-agent results, existing dense monocular SLAM pipelines share two limitations that hinder multi-agent outdoor setting deployment: (i) dependence on precise, fixed intrinsics that are hard to obtain or maintain across heterogeneous robot teams, and (ii) inherent per-agent scale ambiguity that prevents direct map alignment and fusion. Without reliable dense cross-view correspondences and a soft scale anchor, monocular dense SLAM cannot scale to collaborative settings.

### 2.3 Foundation Models and Learned 3D Priors for Vision

Feed-forward 3D reconstruction networks transform geometry estimation as a learned prediction problem. DUST3R [15] directly regresses dense pointmaps in a common frame without known intrinsics; MAST3R [16] enriches this with dense local descriptors for explicit matching, and MAST3R-SfM [48] extends it to unordered collections. Subsequent foundation models [17, 49, 50, 51] further generalize these priors to many-view and streaming regimes. Building on them, MAST3R-SLAM [18] and VGGT-SLAM [19] show that learned 3D priors can deliver globally consistent dense poses and geometry from monocular RGB alone, yet both assume a single continuous tra-

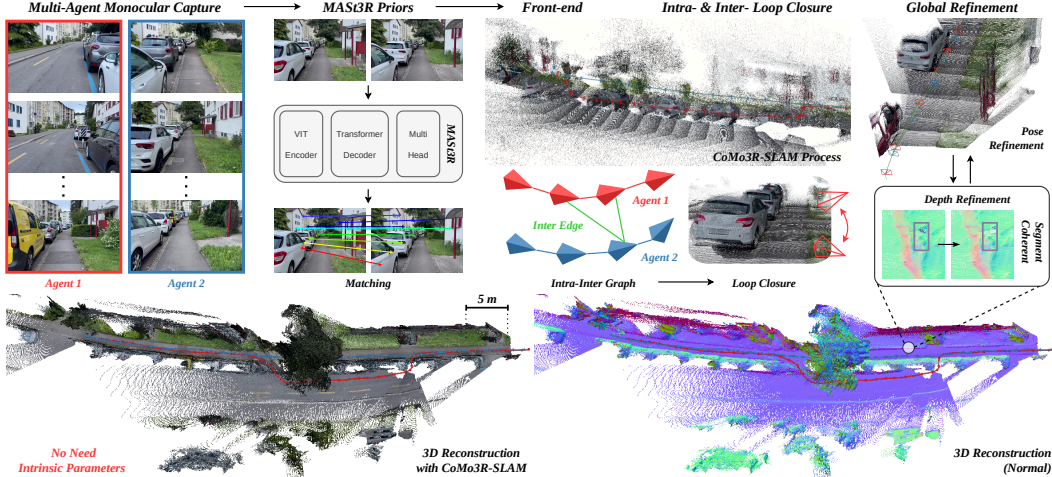


Figure 2: Overview of CoMo3R-SLAM. Each agent runs a prior-guided front-end (Sec. 3.3) that tracks its pose and fuses a local dense pointmap from a monocular RGB stream using a feed-forward 3D reconstruction prior. A central coordinator retrieves candidate cross-agent links over the prior’s encoder features, verifies them by dense symmetric pointmap matching, and synchronizes the agents’ independent gauges with a closed-form Sim(3) alignment (Sec. 3.4). All keyframe poses are jointly refined by a GPU-accelerated global Sim(3) bundle adjustment over a unified multi-agent factor graph and propagated back to every agent (Sec. 3.5).

jectory under one gauge. CoMo3R-SLAM addresses the missing collaborative layer, lifting learned feed-forward 3D reconstruction priors from single-agent to multi-agent outdoor settings. By exploiting the prior’s dense metric pointmaps as soft scale anchors and its geometry-grounded correspondences for robust cross-agent verification, our system achieves reliable inter-agent data association and gauge synchronization under low overlap and large viewpoint changes, capabilities beyond both classical sparse multi-agent SLAM.

### 3 Method

#### 3.1 System Overview

CoMo3R-SLAM is a collaborative dense SLAM system for a team of  $N_a$  robots, each carrying a single monocular RGB camera and producing an independent, asynchronous image stream. The system is organized into a two-level hierarchical architecture. At **Level 1**, every agent runs its own front-end process with learned feed-forward 3D reconstruction prior, which tracks its pose, selects keyframes, fuses a local dense pointmap, and maintains a local Sim(3) keyframe graph (Sec. 3.3). At **Level 2**, a coordinator process receives keyframes from local agents, proposes and verifies cross-agent associations (Sec. 3.4), and runs a global bundle adjustment over the union of all agents’ keyframes (Sec. 3.5). The coordinator periodically broadcasts the globally optimized poses back to the agents, allowing each agent to continue real-time tracking in the shared global frame.

#### 3.2 Learned 3D Priors and the Generic Camera Model

**Feed-forward 3D reconstruction prior.** We use a MAST3R-style two-view prior  $\mathcal{F}$  [16]. Given two images  $I^i, I^j \in \mathbb{R}^{H \times W \times 3}$ , a shared encoder extracts patch tokens, which are then processed by cross-attention decoder heads to produce dense pointmaps  $X_i^i, X_i^j \in \mathbb{R}^{H \times W \times 3}$  for images  $i$  and  $j$ , both expressed in the coordinate frame of camera  $i$ , together with per-pixel geometric confidence  $C_i^i, C_i^j \in \mathbb{R}^{H \times W \times 1}$ , dense  $d$ -dimensional local descriptor field  $D_i^i, D_i^j \in \mathbb{R}^{H \times W \times d}$ , and per-pixel descriptor confidences  $Q_i^i, Q_i^j \in \mathbb{R}^{H \times W \times 1}$ . Since MAST3R is trained with metric-scale supervision whenever metric ground truth is available, its pointmaps provide an approximate learned scale prior. We exploit this prior as a soft anchor for each monocular agent’s gauge, while still allowing residual scale corrections in the global Sim(3) optimization.

**Generic central camera model.** CoMo3R-SLAM makes no assumption about a fixed or parametric camera model beyond a single, common camera centre through which all rays of a frame pass. We convert geometry into a ray representation with the normalization operator  $\psi(X) = \frac{X}{\|X\|}$  and  $\pi(X) = (\psi(X), \|X\|)$ , so a pixel observation is a unit ray  $\psi(X)$  together with a scalar range  $\|X\|$ . This central-camera abstraction handles heterogeneous robot teams equipped with cameras without intrinsics; unless stated otherwise, the method below assumes no calibration, and the optional use of known intrinsics is deferred to Appendix Sec. A.5.

**Pose representation.** Because monocular reconstruction is determined only up to a similarity transform and the learned pointmaps can carry inconsistent scales, every camera pose is a similarity transform  $T = \begin{bmatrix} sR & t \\ \mathbf{0} & 1 \end{bmatrix} \in \text{Sim}(3)$ , with  $R \in \text{SO}(3)$ ,  $t \in \mathbb{R}^3$ , and scale  $s > 0$ . Poses are updated by a left perturbation  $T \leftarrow \text{Exp}(\tau)T$  with Lie algebra  $\tau \in \mathfrak{sim}(3) \cong \mathbb{R}^7$ , and we use analytic Jacobians and tangent-space retraction throughout [52]. Optimizing over  $\text{Sim}(3)$  rather than  $\text{SE}(3)$  makes a per-keyframe scale an explicit degree of freedom, which is the mechanism by which both intra-agent and inter-agent scale are reconciled.

### 3.3 Prior-Guided Per-Agent Front-End

Each agent runs an independent front-end that turns its RGB stream into a local dense map. The front-end is feature-free in the classical sense, where it never detects keypoints, and uses the dense pointmaps and descriptors of the prior for both correspondence and geometry.

**Pointmap matching.** For an incoming frame  $I^f$  and the current keyframe  $I^k$ , the prior predicts the associated pointmaps and descriptors. Rather than a brute-force descriptor search, we obtain a dense pixel correspondence by iterative projective matching on the ray image: each predicted 3D point of  $I^k$  is projected into  $I^f$  by iteratively refining its pixel location  $p$  to minimize the angular ray error [18]

$$p^* = \arg \min_p \|\psi([X_f^f]_p) - \psi(x)\|^2, \quad (1)$$

where  $x \in X_f^k$  is the queried 3D point and  $[\cdot]_p$  denotes pixel-indexed lookup. The match is then refined within a local descriptor window, and the previous frame’s correspondence is reused as initialization for temporal warm-starting. Matches with large 3D discrepancy are rejected as occlusions. This yields a dense set of correspondences  $\mathcal{M}_{kf}$  with per-match confidence  $q_{mn} = \sqrt{Q_{k,m}^k Q_{f,n}^f}$ , where  $m$  indexes the keyframe-side pixel and  $n$  the frame-side pixel, consistent with the residual of Eq. (2).

**Tracking.** Given  $\mathcal{M}_{kf}$ , the relative pose  $T_{kf} \in \text{Sim}(3)$  of the frame with respect to the keyframe is estimated by minimizing a robust ray-and-range residual,

$$E_{\text{track}}(T_{kf}) = \sum_{(m,n) \in \mathcal{M}_{kf}} \sum_{c=1}^4 \rho \left( [\Sigma_{mn}^{-1/2} e_{mn}(T_{kf})]_c \right), \quad e_{mn}(T) = \begin{bmatrix} \psi(T_{kf} X_{f,n}^f) - \psi(\hat{X}_{k,m}^k) \\ \|T_{kf} X_{f,n}^f\| - \|\hat{X}_{k,m}^k\| \end{bmatrix}, \quad (2)$$

where  $\hat{X}_{k,m}^k$  denotes the keyframe’s canonical pointmap fused via a running confidence-weighted average,  $\rho$  is a Huber robust kernel, and  $\Sigma_{mn} = \Sigma/q_{mn}$  with  $\Sigma = \text{diag}(\sigma_r^2 \mathbf{I}_3, \sigma_d^2)$  separately weighting the 3-D ray and 1-D range error per match. The ray term enforces directional consistency under the central-camera model and is bounded against outliers. For robustness, Equation (2) is solved by Levenberg-Marquardt (LM) within an IRLS framework, replacing the Gauss-Newton (GN) solver of [18] while retaining its IRLS reweighting scheme.

**Keyframing and local fusion.** A new keyframe is created when the number of valid matches or unique keyframe pixels falls below a threshold. The keyframe’s canonical pointmap is incrementally fused across all frames that register to it by a confidence-weighted running average,

$$\hat{X}_k^k \leftarrow \frac{\hat{C}_k^k \hat{X}_k^k + C_f^k(T_{kf} X_f^k)}{\hat{C}_k^k + C_f^k}, \quad \hat{C}_k^k \leftarrow \hat{C}_k^k + C_f^k, \quad (3)$$

Table 1: Quantitative comparison of tracking accuracy (ATE RMSE [m]) on the Tanks and Temples dataset [1]. † indicates our system without known calibration. ✗ indicates invalid results due to the failure.

Scene	RGB-D				RGB	
	MAGiC-SLAM [4]	MAC-Ego3D [7]	CP-SLAM [6]	MNE-SLAM [5]	MultiSlam-DiffPose [12]	†CoMo3R-SLAM (Ours)
Barn	0.519	✗	4.972	0.152	0.221	<b>0.051</b>
Caterpillar	0.349	0.361	5.873	0.155	0.148	<b>0.102</b>
Ignatius	0.356	✗	6.178	0.162	0.167	<b>0.144</b>
Truck	0.316	0.374	6.250	0.190	<b>0.035</b>	0.053

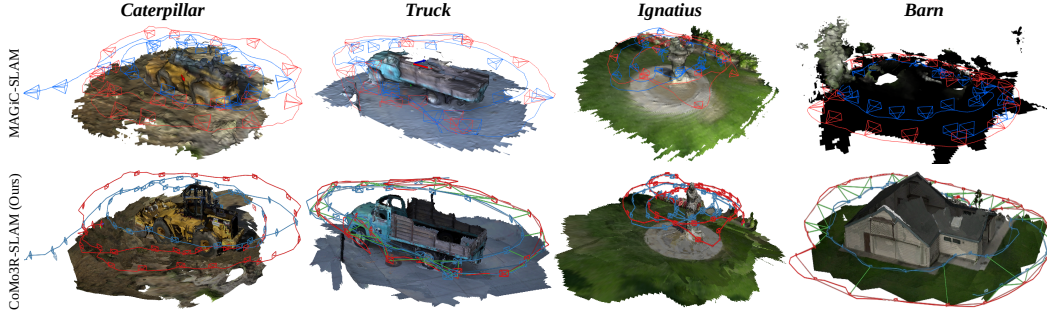


Figure 3: Qualitative comparison of dense reconstructions on the Tanks and Temples dataset [1]. Top: MAGiC-SLAM [4] (RGB-D). Bottom: CoMo3R-SLAM (RGB only). Our method produces comparable or superior reconstruction quality across all four scenes without depth sensors.

which suppresses the noise of any single short-baseline prediction. Each new keyframe is linked to its predecessor by a sequential edge, and intra-agent loop closures are added by querying the agent’s local retrieval database; the resulting per-agent  $\text{Sim}(3)$  keyframe graph is refined by a local LM-IRLS optimization (Appendix Sec. B.2).

### 3.4 Geometrically Verified Cross-Agent Association

The coordinator fuses per-agent maps into a single collaborative map through three stages, including retrieval, geometric verification, and gauge synchronization, via the feed-forward prior  $\mathcal{F}$  from Sec. 3.2, eliminating the need for separate place-recognition or keypoint-detection modules.

**Cross-agent retrieval.** Each keyframe’s encoder tokens are forwarded through the prior’s released HOW-style retrieval head [53] and aggregated into a binary ASMK representation [54] over its pretrained codebook, then inserted into a shared inverted-file database tagged by agent identity. For each new keyframe, top-ranked cross-agent neighbors exceeding a fixed similarity threshold are retained as candidate links; the retrieval-head architecture are detailed in Sec. B.3.

**Geometric verification.** For a candidate pair  $(i, j)$  from agents  $a \neq b$ , the prior decodes both directions to produce dense bidirectional correspondences with validity masks and per-pixel confidence scores  $q_{mn} = \sqrt{Q_{i,m}^i Q_{i,n}^j}$  in each decoded direction. Defining the match fraction  $\nu$  as the proportion of pixels with valid, high-confidence matches in the other view, a candidate is accepted only if  $\min(\nu_i, \nu_j) \geq \tau_{\text{inter}}$ , which rejects one-sided matches and, by operating on the prior’s dense 3D predictions rather than sparse features, handles low overlap and repetitive structures robustly.

**Gauge synchronization.** Each agent’s keyframe chain lives in its own arbitrary frame and scale. One designated agent serves as the global gauge anchor. When a verified edge first connects two previously unsynchronized agents, the coordinator lifts matched canonical points into their respective world frames and solves for the aligning similarity transform via Umeyama [55]:

$$(s^*, R^*, t^*) = \arg \min_{s, R, t} \sum_{(m,n) \in \mathcal{M}_{ij}} \|(sRT_{WC_j} \hat{X}_{j,n}^j + t) - T_{WC_i} \hat{X}_{i,m}^i\|^2, \quad (4)$$

falling back to a rigid snap when correspondences are insufficient. The resulting  $T^* = \begin{bmatrix} s^* R^* & t^* \\ \mathbf{0} & 1 \end{bmatrix} \in \text{Sim}(3)$  is left-multiplied onto every keyframe pose of the unsynchronized agent, transporting its entire chain into the already-synchronized gauge. By anchoring each newly-connected pair on its

lower-indexed agent with agent 0 as the global gauge, all chains are transitively aligned to a single global frame, providing a well-conditioned initialization for global bundle adjustment.

### 3.5 Global Sim(3) Bundle Adjustment over the Multi-Agent Factor Graph

**Unified factor graph.** The coordinator maintains a single factor graph  $\mathcal{G} = (\mathcal{V}, \mathcal{E})$  whose vertices  $\mathcal{V}$  are the Sim(3) poses  $\{T_{WC_i}\}$  of all agents’ keyframes in one flat global index space, each tagged with its agent identity. The edge set  $\mathcal{E} = \mathcal{E}_{\text{intra}} \cup \mathcal{E}_{\text{inter}}$  contains intra-agent sequential edges and the verified inter-agent edges of Sec. 3.4; intra-agent loop closures are resolved within each agent’s local front-end graph (Sec. 3.3) and do not enter the global graph. Every edge, whether intra- or inter-agent, stores the dense pointmap correspondences  $\mathcal{M}_{ij}$ , their validity masks, the canonical pointmaps  $\hat{X}$  of both endpoints, and the per-match confidences  $q_{mn}$  obtained from the prior.

**Pose refinement.** All keyframe poses are refined by minimizing the global ray-and-range energy

$$E_{\text{global}} = \sum_{(i,j) \in \mathcal{E}} \sum_{(m,n) \in \mathcal{M}_{ij}} \sum_{c=1}^4 \rho \left( [\Sigma_{mn}^{-1/2} e_{mn}(T_{ij})]_c \right), \quad T_{ij} = T_{WC_i}^{-1} T_{WC_j}, \quad (5)$$

where  $e_{mn}$  and  $\Sigma_{mn} = \Sigma/q_{mn}$  take the same ray-and-range form and confidence weighting as in Eq. (2). Inter- and intra-agent edges thus contribute identically shaped residuals, fusing cross-agent constraints into a single homogeneous optimization without a separate map-merging stage.

**Segment-level depth refinement.** The optimization above treats each keyframe’s dense geometry as fixed; a final stage refines that geometry as well. Optimizing every pixel’s range independently is under-constrained and prohibitively large, so we adopt a segment-level parameterization, a strategy long used for dense monocular reconstruction [56, 57, 58]: each keyframe is partitioned into a few hundred compact segments whose pixels share a single depth degree of freedom. Segments are obtained by SLIC superpixel clustering [56] applied not to RGB but to prior-derived geometry, where per-pixel surface normals and log-range read from the canonical pointmap, so segment boundaries follow 3D structure. The pixel ranges of segment  $g$  are reparameterized as  $d_p = \|\hat{X}_{k,p}^k\| \exp(s_g)$  with the ray direction  $\psi(\hat{X}_{k,p}^k)$  held fixed within each depth step, leaving one log-scale  $s_g \in \mathbb{R}$  per segment. The stacked log-scales are solved by Gauss-Newton from the same dense residuals as Eq. (5), now including the verified inter-agent edges, so cross-agent correspondences directly constrain structure through the per-segment scalars, augmented by a boundary term that ties adjacent segments’ depth ratios to the prior’s prediction and a prior term anchoring the scales toward the learned geometry. Because pose and structure are coupled through the cross-agent constraints, the terminal refinement alternates a pose LM-IRLS step (Appendix Eq. (25), geometry frozen) with a depth LM-IRLS step (Appendix Eq. (24), poses frozen) until both converge.

## 4 Experiments

We evaluate CoMo3R-SLAM on outdoor multi-agent benchmarks against state-of-the-art RGB-D and RGB collaborative dense SLAM. Full implementation details, additional ablations on known calibration, and a day/night robustness study are deferred to the supplementary material.

**Datasets, baselines, and metric.** We evaluate on Tanks and Temples (T&T) [1] and Waymo [59] outdoor scenes. For both benchmarks, each sequence is split into two sub-trajectories with narrow overlap, simulating two agents observing the same scene independently. We compare against four RGB-D collaborative dense SLAM systems, including MAGiC-SLAM [4], MAC-Ego3D [7], CP-SLAM [6], MNE-SLAM [5], and one RGB multi-agent system, MultiSlam-DiffPose [12]. Tracking accuracy is measured by ATE RMSE [m] after global alignment to ground truth. Unless otherwise noted, all baselines assume known camera intrinsics, whereas our system operates without known intrinsics. Best results are highlighted as **first**, **second**, and **third**.

**Tanks and Temples.** Table 1 reports per-scene ATE on T&T. CoMo3R-SLAM achieves the best ATE on Barn (0.051 m), Caterpillar (0.102 m), and Ignatius (0.144 m), and the second-best on Truck.

Table 2: Quantitative comparison of tracking accuracy (ATE RMSE [m]) on the autonomous driving Waymo dataset [59]. † indicates our system without known calibration. ✗ indicates invalid results due to the failure.

Scene	RGB-D				RGB	
	MAGiC-SLAM [4]	MAC-Ego3D [7]	CP-SLAM [6]	MNE-SLAM [5]	MultiSlam-DiffPose [12]	†CoMo3R-SLAM (Ours)
158686	2.269	6.063	12.277	1.849	1.808	<b>1.773</b>
134763	1.276	3.506	10.287	<b>1.173</b>	2.607	1.965
153495	7.846	8.827	✗	<b>2.811</b>	✗	3.491
106762	14.441	26.867	32.641	5.013	✗	<b>5.004</b>

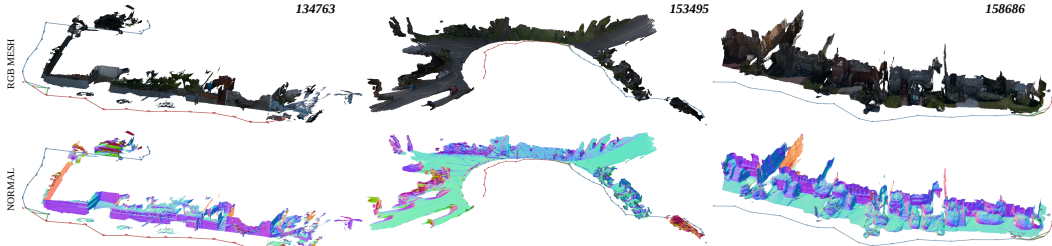


Figure 4: Dense reconstruction results of CoMo3R-SLAM on three Waymo driving scenes [59]. Each column shows the fused RGB reconstructed mesh, and surface normals, demonstrating coherent large-scale outdoor geometry from monocular RGB input alone.

Despite using only RGB and no known intrinsics, our system outperforms all four RGB-D baselines on three of four scenes, and is more than an order of magnitude more accurate than the closest RGB competitor on Barn and Caterpillar. Our dense and geometry-grounded pointmap verification accepts these difficult inter-agent edges only when both directions of the prior agree, and the closed-form Umeyama gauge synchronization then transports the second agent’s chain into the anchor’s gauge with a metric-consistent scale, yielding well-conditioned cross-agent constraints for the subsequent Sim(3) bundle adjustment. The qualitative comparison in Figure 3 confirms that this pose accuracy translates into reconstruction quality: against the RGB-D MAGiC-SLAM, our monocular meshes are comparable or denser in surface coverage and recover fine structure (Truck wheels, Ignatius statue) without any depth sensor.

**Waymo.** Table 2 reports ATE on Waymo. The driving scenes are substantially harder than T&T due to forward-dominant motion, very low parallax, large absolute scale, and highly repetitive street structure. CP-SLAM diverges entirely on 153495, MultiSlam-DiffPose fails on both 153495 and 106762, and even the best RGB-D method degrades by an order of magnitude relative to its T&T performance. CoMo3R-SLAM is the best method overall on 158686 (1.773 m) and 106762 (5.004 m), and remains competitive with RGB-D baseline MNE-SLAM on 134763 and 153495. We attribute this to two mechanisms working together: the soft metric prior carried by the MAST3R pointmaps prevents the per-agent gauges from drifting in scale during long, forward-dominant stretches with little parallax, while the Sim(3) bundle adjustment redistributes the residual scale through the inter-agent edges rather than locking it to a brittle initial guess. Figure 4 visualizes the fused reconstructions and surface normals on three Waymo scenes, showing coherent road surfaces, building façades, and vegetation recovered from monocular input alone over hundreds of metres of driving.

## 5 Conclusion

We presented CoMo3R-SLAM, the first collaborative monocular dense SLAM framework that places learned feed-forward 3D reconstruction priors at the core of outdoor multi-agent mapping. A two-level hierarchical architecture pairs prior-guided per-agent front-ends with a central coordinator that performs prior-feature retrieval, dense pointmap verification, closed-form Sim(3) gauge synchronization, and GPU-accelerated global Sim(3) bundle adjustment over a unified multi-agent factor graph with segment-level depth refinement. On Tanks and Temples and Waymo, CoMo3R-SLAM achieves trajectory accuracy and dense reconstruction quality competitive with, and on most scenes superior to, state-of-the-art RGB-D collaborative systems, all from monocular RGB input without known intrinsics and at approximately 8 FPS.

**Limitations and Future Work.** Two limitations remain. First, the system assumes a single, common camera centre and inherits the training-data statistics of the underlying 3D prior; strongly non-central or heavily distorted optics (e.g. wide-angle fisheye, catadioptric cameras) fall outside this regime. Second, the coordinator-based design prioritises simplicity and global consistency but ties communication load and fault tolerance to a single process as the team scales. Future work includes (i) adapting the 3D prior to wide-FoV and fisheye imagery, and (ii) extending to a fully peer-to-peer formulation where neighbouring agents exchange compressed pointmap summaries and run local sub-graph bundle adjustment, removing the single-aggregation-point dependency.

## References

- [1] A. Knapitsch, J. Park, Q.-Y. Zhou, and V. Koltun. Tanks and temples: Benchmarking large-scale scene reconstruction. *ACM Transactions on Graphics (ToG)*, 36(4):1–13, 2017.
- [2] P. Schmuck, T. Ziegler, M. Karrer, J. Perraudin, and M. Chli. Covins: Visual-inertial slam for centralized collaboration. *arXiv preprint arXiv:2108.05756*, 2021.
- [3] Y. Tian, Y. Chang, F. H. Arias, C. Nieto-Granda, J. P. How, and L. Carlone. Kimera-multi: Robust, distributed, dense metric-semantic slam for multi-robot systems. *IEEE transactions on robotics*, 38(4), 2022.
- [4] V. Yugay, T. Gevers, and M. R. Oswald. Magic-slam: Multi-agent gaussian globally consistent slam. In *Proceedings of the Computer Vision and Pattern Recognition Conference*, pages 6741–6750, 2025.
- [5] T. Deng, G. Shen, C. Xun, S. Yuan, T. Jin, H. Shen, Y. Wang, J. Wang, H. Wang, D. Wang, et al. Mne-slam: Multi-agent neural slam for mobile robots. In *Proceedings of the Computer Vision and Pattern Recognition Conference*, pages 1485–1494, 2025.
- [6] J. Hu, M. Mao, H. Bao, G. Zhang, and Z. Cui. Cp-slam: Collaborative neural point-based slam system. *Advances in Neural Information Processing Systems*, 36:39429–39442, 2023.
- [7] X. Xu, F. Xue, S. Zhao, Y. Pan, S. Scherer, and X. Huang. Mac-ego3d: Multi-agent gaussian consensus for real-time collaborative ego-motion and photorealistic 3d reconstruction. In *Proceedings of the Computer Vision and Pattern Recognition Conference*, pages 854–863, 2025.
- [8] L. Chen, Y. Su, J. Wang, P. Han, Z. Xia, S. Bu, K. Li, B. Hu, S. Meng, and G. Wang. Coma-slam: Collaborative multi-agent gaussian slam with geometric consistency. In *Proceedings of the AAAI Conference on Artificial Intelligence*, volume 40, pages 2922–2929, 2026.
- [9] T. Deng, G. Shen, X. Chen, S. Yuan, H. Shen, G. Peng, Z. Wu, J. Wang, L. Xie, D. Wang, et al. Mcn-slam: Multi-agent collaborative neural slam with hybrid implicit neural scene representation. *arXiv preprint arXiv:2506.18678*, 2025.
- [10] A. Thomas, A. Sonawalla, A. Rose, and J. P. How. Grand-slam: Local optimization for globally consistent large-scale multi-agent gaussian slam. *IEEE Robotics and Automation Letters*, 2025.
- [11] P. Schmuck and M. Chli. Ccm-slam: Robust and efficient centralized collaborative monocular simultaneous localization and mapping for robotic teams. *Journal of Field Robotics*, 36(4): 763–781, 2019.
- [12] L. Lipson and J. Deng. Multi-session slam with differentiable wide-baseline pose optimization. In *Proceedings of the IEEE/CVF Conference on Computer Vision and Pattern Recognition*, pages 19626–19635, 2024.
- [13] Y. Zhou and H. Wu. Multi-agent monocular dense slam with 3d reconstruction priors. *arXiv preprint arXiv:2511.19031*, 2025.
- [14] Y. Li, P. Ye, and Q. Jia. Mang-slam: Multi-agent neural submap and gaussian representation for dense mapping. *IEEE Robotics and Automation Letters*, 11(2):2242–2249, 2025.
- [15] S. Wang, V. Leroy, Y. Cabon, B. Chidlovskii, and J. Revaud. Dust3r: Geometric 3d vision made easy. In *Proceedings of the IEEE/CVF conference on computer vision and pattern recognition*, pages 20697–20709, 2024.
- [16] V. Leroy, Y. Cabon, and J. Revaud. Grounding image matching in 3d with mast3r. In *European conference on computer vision*, pages 71–91. Springer, 2024.

- [17] J. Wang, M. Chen, N. Karaev, A. Vedaldi, C. Rupprecht, and D. Novotny. Vggt: Visual geometry grounded transformer. In *Proceedings of the Computer Vision and Pattern Recognition Conference*, pages 5294–5306, 2025.
- [18] R. Murai, E. Dexheimer, and A. J. Davison. Mast3r-slam: Real-time dense slam with 3d reconstruction priors. In *Proceedings of the Computer Vision and Pattern Recognition Conference*, pages 16695–16705, 2025.
- [19] D. Maggio, H. Lim, and L. Carlone. Vggt-slam: Dense rgb slam optimized on the sl (4) manifold. *Advances in Neural Information Processing Systems*, 38:129839–129867, 2026.
- [20] P.-Y. Lajoie, B. Ramtoula, Y. Chang, L. Carlone, and G. Beltrame. Door-slam: Distributed, online, and outlier resilient slam for robotic teams. *IEEE Robotics and Automation Letters*, 5(2):1656–1663, 2020.
- [21] P.-Y. Lajoie and G. Beltrame. Swarm-slam: Sparse decentralized collaborative simultaneous localization and mapping framework for multi-robot systems. *IEEE Robotics and Automation Letters*, 9(1):475–482, 2023.
- [22] M. M. Li, P.-Y. Lajoie, J. Liu, and G. Beltrame. Compact keyframe-optimized multi-agent gaussian splatting slam. *arXiv preprint arXiv:2604.00804*, 2026.
- [23] J. Yu, T. Chen, and M. Schwager. Hammer: heterogeneous, multi-robot semantic gaussian splatting. *IEEE Robotics and Automation Letters*, 2025.
- [24] Z. Cao, Q. Shao, S. Zhai, J. Zhang, A. Nguyen, and B. Huang. Mags-slam: Monocular multi-agent gaussian splatting slam for geometrically and photometrically consistent reconstruction. *arXiv preprint arXiv:2605.10760*, 2026.
- [25] A. J. Davison, I. D. Reid, N. D. Molton, and O. Stasse. Monoslam: Real-time single camera slam. *IEEE transactions on pattern analysis and machine intelligence*, 29(6):1052–1067, 2007.
- [26] C. Campos, R. Elvira, J. J. G. Rodríguez, J. M. Montiel, and J. D. Tardós. Orb-slam3: An accurate open-source library for visual, visual–inertial, and multimap slam. *IEEE transactions on robotics*, 37(6):1874–1890, 2021.
- [27] J. Engel, T. Schöps, and D. Cremers. Lsd-slam: Large-scale direct monocular slam. In *European conference on computer vision*, pages 834–849. Springer, 2014.
- [28] J. Engel, V. Koltun, and D. Cremers. Direct sparse odometry. *IEEE transactions on pattern analysis and machine intelligence*, 40(3):611–625, 2017.
- [29] R. A. Newcombe, S. J. Lovegrove, and A. J. Davison. Dtam: Dense tracking and mapping in real-time. In *2011 international conference on computer vision*, pages 2320–2327. IEEE, 2011.
- [30] Z. Teed and J. Deng. Droid-slam: Deep visual slam for monocular, stereo, and rgb-d cameras. *Advances in neural information processing systems*, 34:16558–16569, 2021.
- [31] L. Lipson, Z. Teed, and J. Deng. Deep patch visual slam. In *European Conference on Computer Vision*, pages 424–440. Springer, 2024.
- [32] B. Mildenhall, P. P. Srinivasan, M. Tancik, J. T. Barron, R. Ramamoorthi, and R. Ng. Nerf: Representing scenes as neural radiance fields for view synthesis. *Communications of the ACM*, 65(1):99–106, 2021.
- [33] E. Sucar, S. Liu, J. Ortiz, and A. J. Davison. imap: Implicit mapping and positioning in real-time. In *Proceedings of the IEEE/CVF international conference on computer vision*, pages 6229–6238, 2021.

- [34] Z. Zhu, S. Peng, V. Larsson, W. Xu, H. Bao, Z. Cui, M. R. Oswald, and M. Pollefeys. Nice-slam: Neural implicit scalable encoding for slam. In *Proceedings of the IEEE/CVF conference on computer vision and pattern recognition*, pages 12786–12796, 2022.
- [35] Z. Zhu, S. Peng, V. Larsson, Z. Cui, M. R. Oswald, A. Geiger, and M. Pollefeys. Nicer-slam: Neural implicit scene encoding for rgb slam. In *2024 International Conference on 3D Vision (3DV)*, pages 42–52. IEEE, 2024.
- [36] M. M. Johari, C. Carta, and F. Fleuret. Eslam: Efficient dense slam system based on hybrid representation of signed distance fields. In *Proceedings of the IEEE/CVF conference on computer vision and pattern recognition*, pages 17408–17419, 2023.
- [37] E. Sandström, Y. Li, L. Van Gool, and M. R. Oswald. Point-slam: Dense neural point cloud-based slam. In *Proceedings of the IEEE/CVF international conference on computer vision*, pages 18433–18444, 2023.
- [38] L. Liso, E. Sandström, V. Yugay, L. Van Gool, and M. R. Oswald. Loopy-slam: Dense neural slam with loop closures. In *Proceedings of the IEEE/CVF conference on computer vision and pattern recognition*, pages 20363–20373, 2024.
- [39] B. Kerbl, G. Kopanas, T. Leimkühler, G. Drettakis, et al. 3d gaussian splatting for real-time radiance field rendering. *ACM Trans. Graph.*, 42(4):139–1, 2023.
- [40] N. Keetha, J. Karhade, K. M. Jatavallabhula, G. Yang, S. Scherer, D. Ramanan, and J. Luiten. Splatam: Splat track & map 3d gaussians for dense rgb-d slam. In *Proceedings of the IEEE/CVF conference on computer vision and pattern recognition*, pages 21357–21366, 2024.
- [41] E. Sandström, G. Zhang, K. Tateno, M. Oechsle, M. Niemeyer, Y. Zhang, M. Patel, L. Van Gool, M. Oswald, and F. Tombari. Splat-slam: Globally optimized rgb-only slam with 3d gaussians. In *Proceedings of the Computer Vision and Pattern Recognition Conference*, pages 1680–1691, 2025.
- [42] W. Zhang, Q. Cheng, D. Skuddis, N. Zeller, D. Cremers, and N. Haala. Hi-slam2: Geometry-aware gaussian slam for fast monocular scene reconstruction. *IEEE Transactions on Robotics*, 41:6478–6493, 2025.
- [43] M. Li, S. Liu, H. Zhou, G. Zhu, N. Cheng, T. Deng, and H. Wang. Sgs-slam: Semantic gaussian splatting for neural dense slam. In *European Conference on Computer Vision*, pages 163–179. Springer, 2024.
- [44] V. Yugay, Y. Li, T. Gevers, and M. R. Oswald. Gaussian-slam: Photo-realistic dense slam with gaussian splatting. *arXiv preprint arXiv:2312.10070*, 2023.
- [45] H. Matsuki, R. Murai, P. H. Kelly, and A. J. Davison. Gaussian splatting slam. In *Proceedings of the IEEE/CVF conference on computer vision and pattern recognition*, pages 18039–18048, 2024.
- [46] Z. Peng, T. Shao, Y. Liu, J. Zhou, Y. Yang, J. Wang, and K. Zhou. Rtg-slam: Real-time 3d reconstruction at scale using gaussian splatting. In *ACM SIGGRAPH 2024 conference papers*, pages 1–11, 2024.
- [47] Z. Cao, H. Wu, L. W. Tang, Z. Luo, W. Zhang, M. Pollefeys, Z. Zhu, and M. R. Oswald. Mcgs-slam: A multi-camera slam framework using gaussian splatting for high-fidelity mapping. *arXiv preprint arXiv:2509.14191*, 2025.
- [48] B. P. Duisterhof, L. Zust, P. Weinzaepfel, V. Leroy, Y. Cabon, and J. Revaud. Mast3r-sfm: a fully-integrated solution for unconstrained structure-from-motion. In *2025 International Conference on 3D Vision (3DV)*, pages 1–10. IEEE, 2025.

- [49] Q. Wang, Y. Zhang, A. Holynski, A. A. Efros, and A. Kanazawa. Continuous 3d perception model with persistent state. In *Proceedings of the Computer Vision and Pattern Recognition Conference*, pages 10510–10522, 2025.
- [50] Y. Liu, S. Dong, S. Wang, Y. Yin, Y. Yang, Q. Fan, and B. Chen. Slam3r: Real-time dense scene reconstruction from monocular rgb videos. In *Proceedings of the Computer Vision and Pattern Recognition Conference*, pages 16651–16662, 2025.
- [51] H. Wang and L. Agapito. 3d reconstruction with spatial memory. In *2025 International Conference on 3D Vision (3DV)*, pages 78–89. IEEE, 2025.
- [52] Z. Teed and J. Deng. Tangent space backpropagation for 3d transformation groups. In *Proceedings of the IEEE/CVF conference on computer vision and pattern recognition*, pages 10338–10347, 2021.
- [53] G. Tolas, T. Jenicek, and O. Chum. Learning and aggregating deep local descriptors for instance-level recognition. In *European Conference on Computer Vision*, pages 460–477. Springer, 2020.
- [54] G. Tolas, Y. Avrithis, and H. Jégou. To aggregate or not to aggregate: Selective match kernels for image search. In *Proceedings of the IEEE international conference on computer vision*, pages 1401–1408, 2013.
- [55] S. Umeyama. Least-squares estimation of transformation parameters between two point patterns. *IEEE Transactions on pattern analysis and machine intelligence*, 13(4):376–380, 1991.
- [56] R. Achanta, A. Shaji, K. Smith, A. Lucchi, P. Fua, and S. Süsstrunk. Slic superpixels compared to state-of-the-art superpixel methods. *IEEE transactions on pattern analysis and machine intelligence*, 34(11):2274–2282, 2012.
- [57] A. Concha and J. Civera. Dpptom: Dense piecewise planar tracking and mapping from a monocular sequence. In *2015 IEEE/RSJ International Conference on Intelligent Robots and Systems (IROS)*, pages 5686–5693. IEEE, 2015.
- [58] K. Mazur, G. Bae, and A. J. Davison. Superprimitive: Scene reconstruction at a primitive level. In *Proceedings of the IEEE/CVF Conference on Computer Vision and Pattern Recognition*, pages 4979–4989, 2024.
- [59] P. Sun, H. Kretzschmar, X. Dotiwalla, A. Chouard, V. Patnaik, P. Tsui, J. Guo, Y. Zhou, Y. Chai, B. Caine, et al. Scalability in perception for autonomous driving: Waymo open dataset. In *Proceedings of the IEEE/CVF conference on computer vision and pattern recognition*, pages 2446–2454, 2020.

## Appendix / Supplemental Materials

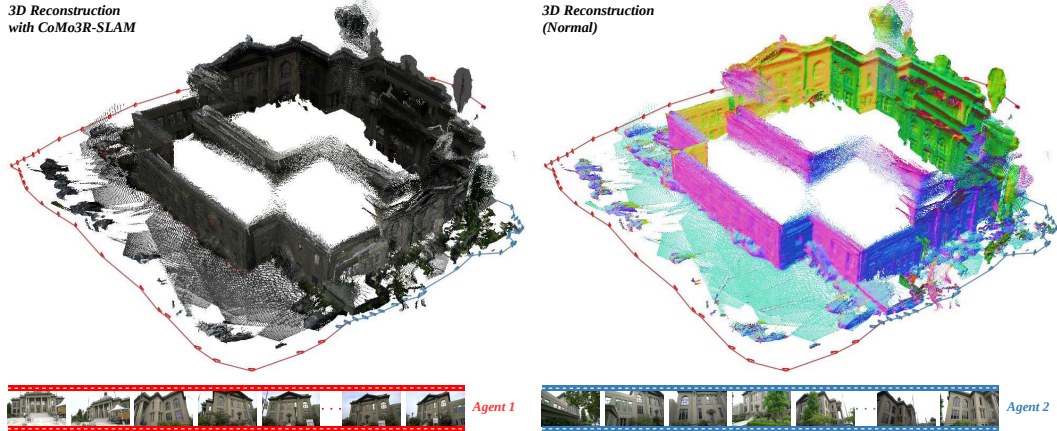


Figure 5: CoMo3R-SLAM performs collaborative monocular dense SLAM from two RGB-only agent streams on the outdoor Courthouse scene [1]. Given monocular image sequences with limited cross-agent overlap, our system estimates globally aligned camera trajectories, establishes inter-agent constraints, and reconstructs a consistent dense scene geometry without depth sensors.

### A Additional Methodology Details

This section provides the formulas, derivations, and algorithmic specifics that the main paper omits due to space. It expands on the per-agent residuals (Sec. A.1) and their analytical Jacobians on Sim(3) (Sec. A.2); makes the multi-agent factor-graph notation explicit (Sec. A.3); writes the closed-form gauge synchronization and its fallback (Sec. A.4); completes the known-calibration variant (Sec. A.5); and gives the full segment-level depth refinement together with the terminal pose-depth alternation (Sec. A.6 to Sec. A.7). The final paragraph (Sec. A.8) details how the globally-optimized poses are propagated back to each agent.

#### A.1 Ray-and-Range Residuals and Per-Match Weighting

The tracking energy of Eq. (2) and the global energy of Eq. (5) share a common per-match residual

$$e_{mn}(T) = \begin{bmatrix} \psi(TX_{j,n}^j) - \psi(\hat{X}_{i,m}^i) \\ \|TX_{j,n}^j\| - \|\hat{X}_{i,m}^i\| \end{bmatrix} \in \mathbb{R}^4, \quad (6)$$

whose unit-ray component lies on the unit 2-sphere, which is a 2-dimensional submanifold of  $\mathbb{R}^3$ . Therefore, its three entries carry only two intrinsic degrees of freedom. We keep the redundant 3-vector form because the projector that appears in the analytical Jacobian (Eq. (10)) makes this rank-2 structure explicit at the linearisation level and preserves the closed-form Jacobian block used below. The diagonal covariance

$$\Sigma_{mn} = \frac{1}{q_{mn}} \Sigma, \quad \Sigma = \text{diag}(\sigma_r^2 \mathbf{I}_3, \sigma_d^2), \quad q_{mn} = \sqrt{Q_{j,n}^j Q_{i,m}^i}, \quad (7)$$

separates the angular noise  $\sigma_r$  of a ray observation from the metric noise  $\sigma_d$  of a range observation, and divides by the geometric mean of the two endpoint descriptor confidences so that the prior's own uncertainty modulates the influence of each match. The robust energies of Eqs. (2) and (5) apply the Huber kernel  $\rho(\cdot)$  of breakpoint  $k = 1.345$  independently to each entry of the whitened residual; the per-match contribution

$$\sum_{c=1}^4 \rho([\Sigma_{mn}^{-1/2} e_{mn}]_c) \quad (8)$$

lets ray and range outliers be downweighted independently, which is important because the prior's directional and metric noise can fail in markedly different regimes (e.g. a textureless surface yields

a sharp ray but an unreliable range). Each scalar component thus carries its own IRLS weight  $w(r_c) = \min(1, k/|r_c|)$ , absorbed into the diagonal of the square-root information  $\Sigma_{mn}^{-1/2}$  at every iteration of the solver of Sec. B.2.

## A.2 Analytical Jacobians on Sim(3)

All solvers in CoMo3R-SLAM use the left-perturbation retraction  $T \leftarrow \text{Exp}(\tau)T$  of Sec. 3.2 with  $\tau = (\mathbf{v}, \boldsymbol{\omega}, \zeta) \in \mathfrak{sim}(3)$ , where  $\mathbf{v} \in \mathbb{R}^3$  is the translation perturbation,  $\boldsymbol{\omega} \in \mathbb{R}^3$  the rotation perturbation, and  $\zeta \in \mathbb{R}$  the log-scale perturbation. Writing  $\mathbf{x} = TX$  with  $d_x = \|\mathbf{x}\|$ , the directional derivative of a transformed point with respect to  $\tau$  is

$$\frac{D\mathbf{x}}{D\tau} = [\mathbf{I}_3 \quad -[\mathbf{x}]_{\times} \quad \mathbf{x}] \in \mathbb{R}^{3 \times 7}, \quad (9)$$

which is the same block used by the original MAST3R-SLAM derivation [18]. The unit-ray and range Jacobians follow by the chain rule:

$$\frac{D\psi(\mathbf{x})}{D\mathbf{x}} = \frac{1}{d_x} \left( \mathbf{I}_3 - \frac{\mathbf{x}\mathbf{x}^{\top}}{d_x^2} \right), \quad \frac{Dd_x}{D\mathbf{x}} = \frac{\mathbf{x}^{\top}}{d_x}. \quad (10)$$

Writing the per-match residual of Eq. (6) as  $e_{mn} = (e_{\psi}^{\top}, e_d)^{\top}$  with the unit-ray block  $e_{\psi} = \psi(TX_{j,n}^j) - \psi(\hat{X}_{i,m}^i) \in \mathbb{R}^3$  and the range scalar  $e_d = \|TX_{j,n}^j\| - \|\hat{X}_{i,m}^i\| \in \mathbb{R}$ , the chain rule yields  $\partial e_{\psi}/\partial\tau \in \mathbb{R}^{3 \times 7}$  and  $\partial e_d/\partial\tau \in \mathbb{R}^{1 \times 7}$  that are stacked into a  $4 \times 7$  block per match. For a relative-pose edge  $T_{ij} = T_{WC_i}^{-1} T_{WC_j}$ , the contribution of  $\tau$  at the two endpoints follows from the Sim(3) adjoint  $\text{Ad}_T : \mathfrak{sim}(3) \rightarrow \mathfrak{sim}(3)$  defined by  $T \exp(\xi) T^{-1} = \exp(\text{Ad}_T \xi)$  [52],

$$\frac{DT_{ij}}{DT_{WC_i}} = -\text{Ad}_{T_{WC_i}^{-1}}, \quad \frac{DT_{ij}}{DT_{WC_j}} = +\text{Ad}_{T_{WC_i}^{-1}}, \quad (11)$$

so that every edge contributes the same residual block to two  $7 \times 7$  diagonal Hessian entries and one off-diagonal block, regardless of whether the edge is intra-agent or inter-agent. This sparsity pattern is what allows the solver of Sec. B.2 to scale to the unified multi-agent factor graph at a constant per-edge cost.

## A.3 Unified Multi-Agent Factor Graph

The coordinator maintains a single factor graph  $\mathcal{G} = (\mathcal{V}, \mathcal{E})$  whose vertices  $i \in \mathcal{V}$  are addressed in a single flat global index space  $\{0, 1, \dots, N-1\}$ , where  $N = \sum_{a=0}^{N_a-1} N_a^{\text{kf}}$  is the total number of keyframes across all agents. A side map  $a(i) \in \{0, 1, \dots, N_a - 1\}$  records the originating agent identity of vertex  $i$ , and each agent  $a$  keeps a private local-to-global map so that its front-end can address its own keyframes both by local index (for local fusion) and by global index (for the coordinator's solves). The edge set is  $\mathcal{E} = \mathcal{E}_{\text{intra}} \cup \mathcal{E}_{\text{inter}}$ , including

$$\mathcal{E}_{\text{intra}} = \{(i, j) | a(i) = a(j), \alpha(i, j) = 1\}, \quad \mathcal{E}_{\text{inter}} = \{(i, j) | a(i) \neq a(j), \nu(i, j) = 1\}, \quad (12)$$

where the admission predicate  $\alpha(\cdot, \cdot)$  selects the per-agent sequential edges that have been promoted to the global graph and  $\nu(\cdot, \cdot)$  selects the geometrically-verified cross-agent edges of Sec. 3.4; intra-agent loop closures are resolved inside each agent's local LM-IRLS solve (Sec. 3.3) and do not enter  $\mathcal{E}$ . Every edge, irrespective of class, stores the same payload: the two endpoints' canonical pointmaps  $\hat{X}_i^i, \hat{X}_j^j$ , the dense correspondence index sets  $\mathcal{M}_{ij}, \mathcal{M}_{ji}$  with their validity masks, and the per-match confidences  $q_{mn}$ . The global energy of Eq. (5) then expresses the relative pose as

$$T_{ij} = T_{WC_i}^{-1} T_{WC_j}, \quad \forall (i, j) \in \mathcal{E}, \quad (13)$$

so intra- and inter-agent edges contribute residuals of identical shape. To remove the global Sim(3) gauge freedom, the keyframe at global index 0 (the first keyframe of the anchor agent) is held fixed; only the remaining  $N - 1$  poses are updated.

#### A.4 Closed-Form Gauge Synchronization and Rigid-Snap Fallback

When a verified inter-agent edge first connects two agents that have not yet been gauge-aligned, the coordinator transports the entire keyframe chain of the higher-indexed agent into the gauge of the lower-indexed one. Let  $\{(\mathbf{x}_k, \mathbf{y}_k)\}_{k=1}^{N_c}$  denote the matched pairs of canonical points lifted into their respective world frames, with centroids  $\bar{\mathbf{x}}, \bar{\mathbf{y}}$  and centered point sets  $\tilde{\mathbf{x}}_k, \tilde{\mathbf{y}}_k$ . Defining the cross-covariance  $\Sigma_{xy} = \frac{1}{N_c} \sum_k \tilde{\mathbf{x}}_k \tilde{\mathbf{y}}_k^\top$  with SVD  $\Sigma_{xy} = U\Lambda V^\top$  and the proper-rotation diagonal  $D = \text{diag}(1, 1, \det(UV^\top))$ , the optimal similarity transform from agent  $b$ 's frame to agent  $a$ 's frame is given in closed form [55] by

$$R^* = UDV^\top, \quad s^* = \frac{\text{tr}(DA)}{\frac{1}{N_c} \sum_k \|\tilde{\mathbf{y}}_k\|^2}, \quad t^* = \bar{\mathbf{x}} - s^* R^* \bar{\mathbf{y}}. \quad (14)$$

The resulting similarity  $T^* = \begin{bmatrix} s^* R^* & t^* \\ \mathbf{0} & 1 \end{bmatrix} \in \text{Sim}(3)$  is left-multiplied onto every keyframe pose of the unsynchronized agent,

$$T_{WC_i} \leftarrow T^* T_{WC_i}, \quad \forall i \text{ with } a(i) = b, \quad (15)$$

so that the moving agent's full chain enters the anchor's gauge in a single transport step. The closed-form solver requires a minimum of  $N_c \geq 64$  high-confidence correspondences; below this threshold the SVD is poorly conditioned and the coordinator instead falls back to a rigid snap derived from the two edge endpoints, setting  $T^* = T_{WC_i} T_{WC_j}^{-1}$  and applying it via Eq. (15) to every keyframe of the moving agent. Equivalently, the moving endpoint  $T_{WC_j}$  is snapped to coincide with the anchor endpoint  $T_{WC_i}$ , while the rest of the moving chain is rigidly transported by the same similarity so the chain remains internally consistent; the subsequent global  $\text{Sim}(3)$  bundle adjustment then absorbs the remaining residual misalignment. By always anchoring the lower-indexed agent in each newly-connected pair, with agent 0 as the root, all chains are transitively transported into a single common gauge, providing a well-conditioned initialization for the optimization of Sec. B.2.

#### A.5 Known Calibration

The method above assumes no camera intrinsics, where every residual, association, and optimization operates purely on the rays and ranges predicted by the learned prior. When a per-agent calibration  $K = \begin{bmatrix} f_x & 0 & c_x \\ 0 & f_y & c_y \\ 0 & 0 & 1 \end{bmatrix}$  is available, CoMo3R-SLAM exploits it through two localized changes that leave the architecture, the factor graph, and the solvers untouched. First, before a keyframe's canonical pointmap enters tracking, the global bundle adjustment, or the depth refinement, it is constrained to the rays defined by  $K$ : only the predicted range  $z_p$  is retained, while each pixel's bearing is locked to the calibrated pixel grid,

$$\hat{X}_p \leftarrow z_p K^{-1} \begin{bmatrix} u_p \\ v_p \\ 1 \end{bmatrix}, \quad z_p = [\hat{X}_p]_3, \quad (16)$$

so the pointmap collapses to a per-pixel depth living on the calibrated ray bundle. Second, the unit-ray and range components of  $e_{mn}$  in Eq. (6) are replaced by a pixel-reprojection error and a log-depth error, both evaluated at the calibrated projection  $\Pi_K(\mathbf{x}) = [(f_x x + c_x z)/z, (f_y y + c_y z)/z]^\top$ :

$$e_{mn}^{\text{cal}}(T) = \begin{bmatrix} \Pi_K(TX_{j,n}^j) - \mathbf{p}_{i,m} \\ \log [TX_{j,n}^j]_3 - \log [\hat{X}_{i,m}^i]_3 \end{bmatrix} \in \mathbb{R}^3, \quad (17)$$

where  $\mathbf{p}_{i,m}$  is the observed pixel coordinate in image  $i$ . The Mahalanobis weighting becomes  $\Sigma_{mn}^{\text{cal}} = (1/q_{mn}) \text{diag}(\sigma_p^2 \mathbf{I}_2, \sigma_z^2)$  with a per-pixel reprojection noise  $\sigma_p$  and a per-log-depth noise  $\sigma_z$ ; the component-wise Huber kernel and IRLS reweighting carry over verbatim. Writing  $\mathbf{x} = TX_{j,n}^j = (x, y, z)^\top$ , the calibrated pixel Jacobian needed by the solver is

$$\frac{\partial \Pi_K(\mathbf{x})}{\partial \mathbf{x}} = \frac{1}{z} \begin{bmatrix} f_x & 0 & -f_x x/z \\ 0 & f_y & -f_y y/z \end{bmatrix}, \quad (18)$$

composed with  $D\mathbf{x}/D\tau$  of Eq. (9) to obtain the  $2 \times 7$  contribution to the block Hessian; the log-depth row  $\partial \log z / \partial \mathbf{x} = (0, 0, 1/z)$  is composed with the same  $D\mathbf{x}/D\tau$  to give the remaining  $1 \times 7$  contribution. However, the segment-level depth refinement of Sec. A.6 is left unchanged: its per-segment Gauss-Newton residual and Jacobians are the same expressions in either mode, because calibration only alters the ray basis on which the per-segment log-scales act through Eq. (16). Because the learned prior already supplies metric pointmaps, known intrinsics serve merely to sharpen this ray basis rather than to enable the system, so the uncalibrated and calibrated variants share a single optimization pipeline.

## A.6 Segment-Level Depth Refinement

**Segments from geometry.** Once the pose solve has converged, the coordinator refines the dense geometry of every keyframe; this refinement is then alternated with short pose passes as detailed in Sec. A.7, and each call proceeds as follows. Each canonical pointmap is oversegmented into compact patches whose pixels share a single depth degree of freedom. The segmentation is computed by SLIC [56], but the input channels are not RGB; instead they are the per-pixel surface normals estimated from central differences of the canonical pointmap and the canonical log-range linearly normalised to  $[0, 1]$ , so segment boundaries align with 3D structure rather than appearance. SLIC itself runs on the full normal-and-log-range feature image and is not masked by confidence; after clustering, pixels whose accumulated MAST3R confidence falls below a dedicated threshold  $c_{\text{seg}}$  have their labels overwritten with  $-1$  so that low-confidence regions never enter the per-segment solver. Segment boundaries may therefore still span low-confidence regions, which we allow deliberately to avoid fragmenting the segmentation under spatially noisy confidence; only the low-confidence pixels themselves are excluded from the solve. Segments containing fewer than 16 valid pixels are subsequently dropped into the same invalid mask to avoid ill-conditioned per-segment Newton steps. After relabelling, the  $k$ -th keyframe is associated with  $M_k$  dense, contiguous segment labels indexed by  $g \in \{0, \dots, M_k - 1\}$ .

**Per-segment log-scale parameterisation.** For every valid pixel  $p$  in segment  $g$  of keyframe  $k$ , the refined point is constrained to lie along the prior’s ray with a single multiplicative correction,

$$\hat{X}_{k,p}^k(s_g) = \|\hat{X}_{k,p,\text{init}}^k\| \exp(s_g) \psi(\hat{X}_{k,p,\text{init}}^k), \quad (19)$$

where  $\hat{X}_{k,p,\text{init}}^k$  is the pristine, frozen MAST3R canonical pointmap snapshot taken at the moment the keyframe was first inserted, and  $s_g \in \mathbb{R}$  is the lone unknown for the entire segment. In the calibrated variant of Sec. A.5, the snapshot has already been constrained to the  $K$ -rays via Eq. (16) before the keyframe enters depth refinement, so  $\psi(\hat{X}_{k,p,\text{init}}^k)$  coincides with the calibrated pixel ray and Eq. (19) is unchanged in either mode. Stacking all log-scales over all keyframes yields the global parameter vector  $\mathbf{s} \in \mathbb{R}^M$  with  $M = \sum_k M_k$ , typically two to three orders of magnitude smaller than the per-pixel depth space. Log-space keeps the boundary and prior residuals (Eqs. (22) to (23)) linear in  $\mathbf{s}$ ; the data residual of Eq. (21) remains non-linear in  $\mathbf{s}$  via  $\exp(s_g)$  and is linearised at each Gauss-Newton step, but the log parameterisation keeps both halves immune to  $\exp(\cdot)$  overflow.

**Per-segment Energy.** The refinement minimises a sum of three terms,

$$E_{\text{depth}}(\mathbf{s}) = E_{\text{data}} + \lambda_{\text{smooth}} E_{\text{bnd}} + \lambda_{\text{prior}} E_{\text{prior}}, \quad (20)$$

each computed at frozen poses. Because  $T_{ij}$  is held fixed during depth refinement, the ray component of Eq. (6) contributes only a constant offset; we therefore replace the ray-and-range factor by a 3D-point residual in the source camera frame, evaluated under the parametrisation of Eq. (19), whitened by an isotropic per-component noise  $\sigma_{\text{point}}$  modulated by the same per-match confidence  $q_{mn}$  of Eq. (7), and summed component-wise under Huber over the same intra- and inter-agent edges  $\mathcal{E}$  that the pose solve uses (matches with  $q_{mn} \leq q_{\text{min}}$  are dropped by the same  $Q$ -gate as in the pose solve, while low-confidence endpoint pixels have already been removed upstream by the SLIC-stage pre-filter via the  $-1$  label, so the data residual is evaluated only on valid-label pairs),

$$E_{\text{data}} = \sum_{(i,j) \in \mathcal{E}} \sum_{(m,n) \in \mathcal{M}_{ij}} \sum_{c=1}^3 \rho \left( \frac{\sqrt{q_{mn}} [T_{ij} \hat{X}_{j,n}^j(\mathbf{s}) - \hat{X}_{i,m}^i(\mathbf{s})]_c}{\sigma_{\text{point}}} \right), \quad (21)$$

so cross-agent correspondences constrain structure directly through the per-segment scalars rather than through pose updates. The boundary term operates on the unique unordered 4-adjacent segment pairs  $(a, b)$  of every keyframe, with a representative log-depth ratio  $\Delta_{ab} = \overline{\log d_a^{\text{init}}} - \overline{\log d_b^{\text{init}}}$  averaged across the shared boundary pixels,

$$E_{\text{bnd}} = \sum_{(a,b) \in \mathcal{B}} \left( (s_a - s_b) + \Delta_{ab} \right)^2, \quad (22)$$

which drives the refined log-depths  $\log d_a = \log d_a^{\text{init}} + s_a$  and  $\log d_b = \log d_b^{\text{init}} + s_b$  to agree at the shared boundary; the log-space form makes this residual linear in  $\mathbf{s}$ , scale-invariant, and overflow-free. Finally, the prior term anchors each segment to the learned geometry,

$$E_{\text{prior}} = \sum_{g=1}^M s_g^2, \quad (23)$$

so that in the absence of cross-edge evidence the segment depth defaults to the MAST3R prediction  $s_g = 0 \Rightarrow d_p = d_p^{\text{init}}$ . With both  $\lambda_{\text{smooth}}$  and  $\lambda_{\text{prior}}$  set to 1.0, the boundary and prior contributions are commensurate with the data term under the configured  $\sigma_{\text{point}}$ .

**Per-segment Newton step.** Following the standard Gauss-Newton convention used throughout the paper, the three energies of Eqs. (21) to (23) are written without the conventional  $\frac{1}{2}$  prefactor and the prefactor is absorbed into the solver, so that the prior contributes  $\lambda_{\text{prior}} \mathbf{I}$  to the segment Hessian. The data and boundary terms apply the same Jacobi-style decoupling at the Hessian level: whenever a residual couples two distinct segments  $a, b$ , only the diagonal entries  $J_a^\top W J_a$  and  $J_b^\top W J_b$  of the true  $2 \times 2$  Gauss-Newton block are accumulated into  $H_{\text{seg}}[a]$  and  $H_{\text{seg}}[b]$ , while the off-diagonal cross-segment entry  $J_a^\top W J_b$  is dropped. For the data residual of Eq. (21), the chain-ruled segment Jacobians are  $J_a = -d_i \mathbf{ray}_i$  and  $J_b = d_j (s_{ij} R_{ij} \mathbf{ray}_j)$  at a match  $(m, n) \in M_{ij}$  whose endpoints lie in segments  $a$  (pixel  $m$  of keyframe  $i$ ) and  $b$  (pixel  $n$  of keyframe  $j$ ), so the per-match Hessian splits into the diagonal contributions  $d_i^2 \mathbf{ray}_i^\top W \mathbf{ray}_i$  and  $d_j^2 (s_{ij} R_{ij} \mathbf{ray}_j)^\top W (s_{ij} R_{ij} \mathbf{ray}_j)$  while the cross block  $-d_i d_j \mathbf{ray}_i^\top W (s_{ij} R_{ij} \mathbf{ray}_j)$  is discarded. For the boundary residual  $r_{ab} = (s_a - s_b) + \Delta_{ab}$  the constant Jacobians  $(+1, -1)$  make the diagonal contributions equal to  $\lambda_{\text{smooth}}$  at each of segments  $a$  and  $b$ , and the dropped off-diagonals equal to  $-\lambda_{\text{smooth}}$ . In both cases the cross-segment information is retained in the gradient through the shared residual: the data term adds  $J_a^\top W r$  to  $g_{\text{seg}}[a]$  and  $J_b^\top W r$  to  $g_{\text{seg}}[b]$ , and the boundary term adds  $\pm \lambda_{\text{smooth}} r_{ab}$  at the two endpoints. This Jacobi-style decoupling at the Hessian level reduces the per-iteration solve to independent per-segment  $1 \times 1$  damped-Newton steps (Eq. (24)) that map trivially onto a single GPU pass. The exact gradient is preserved, so the iteration targets the same first-order optimality condition  $g_{\text{seg}} = 0$  as a coupled solver, where only the curvature model used to choose the step direction is approximated; in practice this costs a handful of additional Gauss-Newton iterations against the coupled alternative while removing all inter-segment fill-in from the linear system. After accumulating  $H_{\text{data}}$ ,  $H_{\text{bnd}}$  and  $H_{\text{prior}} \triangleq \lambda_{\text{prior}} \mathbf{I}$  in parallel on the GPU (the prior likewise contributing  $\lambda_{\text{prior}} s_g$  to  $g_{\text{seg}}[g]$ ), the segment-wise normal equation

$$(H_{\text{data}} + H_{\text{bnd}} + H_{\text{prior}}) \Delta \mathbf{s} = -g \quad (24)$$

is solved through the same LM-IRLS pipeline as the pose solve of Sec. B.2, with depth-specific LM damping  $\lambda_{\text{lm}} = 0.05$  on the per-segment  $1 \times 1$  Hessian and a per-iteration step clip  $|\Delta s_g| \leq s_{\text{max}}$  where  $s_{\text{max}} = 0.5$  keeps cumulative  $|s_g|$  bounded so that  $\exp(s_g)$  cannot overflow. Pinned keyframes (e.g. the global anchor) have their segments held fixed; all other segments are updated each iteration. The solver runs for at most 10 inner iterations per call.

## A.7 Alternating Pose-Depth Optimisation at Cleanup

Pose and structure are coupled only through the data term: the boundary and prior terms in Eq. (20) are independent of  $\{T_{WC_i}\}$ , and the global energy of Eq. (5) is independent of  $\mathbf{s}$ . After all agents have terminated, the coordinator therefore exploits this block-coordinate structure with the following schedule:

1. Run global pose LM-IRLS over Eq. (5) (depths frozen) for at most 100 iterations; repeat up to 5 passes until  $\max_i \|\Delta \mathbf{t}_{WC_i}\|_2 < 5\text{mm}$ .
2. For  $r = 1, \dots, R$  with  $R = 100$ :
  - (a) build segments from each keyframe’s current canonical pointmap via Eq. (19);
  - (b) refine  $\mathbf{s}$  by Eq. (24) (poses frozen, 10 inner iterations);
  - (c) write the updated  $\hat{X}$  back into the canonical pointmaps;
  - (d) run a short pose pass (Eq. (5), 50 iterations) so the poses absorb the depth change;
  - (e) broadcast the new global poses to all agents.

The alternation is the smallest schedule that lets each side react to the other while reusing both LM-IRLS solvers verbatim. Each sub-problem is a damped LM step on its own block of variables, and the shared data term keeps the two energies tightly coupled. We do not enforce strict monotonicity in  $E_{\text{global}} + E_{\text{depth}}$  across the alternation, where the pose Gauss-Newton loop applies each computed update without a cost evaluation or rollback, and the per-segment step clip  $|\Delta s_g| \leq s_{\text{max}}$  admits inner sub-steps that do not strictly decrease  $E_{\text{depth}}$ , however, in practice the schedule converges within a handful of rounds across all of our experiments.

## A.8 Global-to-Local Pose Propagation

The global pose solve is triggered once the number of newly admitted inter-agent edges reaches a configurable interval, and the depth refinement runs in the terminal cleanup together with the pose-depth alternation of Sec. A.7. After each solve, including every round of the terminal pose-depth alternation, the coordinator pushes a lightweight pose update message onto the per-agent multiprocessing queue; each agent then overwrites the world poses of its keyframes from the shared global pose buffer through the local-to-global index map of Sec. A.3 (the gauge anchor is pinned during the global solve, so the corresponding write is a no-op), so subsequent front-end tracking is expressed directly in the shared global frame. Each non-keyframe is recorded by its front-end as a tuple (frame\_id,  $k_{\text{anchor}}$ ,  $T^{\text{rel}}$ ), where  $k_{\text{anchor}}$  is the global index of the most recent local keyframe, which is the keyframe the front-end tracked the frame against, and  $T^{\text{rel}} \in \text{Sim}(3)$  is the relative pose computed at tracking time. At trajectory save time the non-keyframe poses are reconstructed as  $T_{WC}^{\text{frame}} = T_{WC, k_{\text{anchor}}} \cdot T^{\text{rel}}$ , so any pose update absorbed by an anchor keyframe is automatically inherited by all of its child frames without a separate broadcast. The result is a set of globally aligned camera trajectories at the full input frame rate over all successfully tracked frames, and a single consistent dense reconstruction for the whole robot team, obtained without any depth sensor.

## B Additional Implementation Details

### B.1 Experimental Setup

CoMo3R-SLAM is implemented in PyTorch with custom CUDA extensions for the GPU-accelerated  $\text{Sim}(3)$  bundle adjustment, the dense pointmap projective matching, and the segment-level depth refinement. Each agent runs as an independent process and communicates with the coordinator only via lightweight keyframe messages over a pair of inter-process queues, where one carrying new-keyframe payloads from each agent to the coordinator, and one carrying pose-update and termination signals from the coordinator back to the agents, therefore, the two agents in our experiments are fully decoupled at runtime and the pipeline scales transparently to additional agents. All experiments are conducted with NVIDIA RTX 3080ti GPUs; the full collaborative system, including both agent front-ends and the coordinator’s retrieval, verification, gauge synchronization, and global  $\text{Sim}(3)$  bundle adjustment, sustains around 8 FPS per agent end-to-end. Unless otherwise noted, the headline numbers in Tables 1 and 2 are produced in the uncalibrated regime, in which the known-calibration switch is disabled; the calibrated ablation of Table 6 enables the same switch without any other change to the pipeline. Hyperparameters used throughout the paper follow the released configuration (Table 3).

## B.2 GPU-Accelerated LM-IRLS Solver

Every Sim(3) optimization in CoMo3R-SLAM, where the per-frame tracker (Eq. (2)), the per-agent local solve (Sec. 3.3), and the global bundle adjustment over Eq. (5), which is performed by the same GPU-accelerated Levenberg-Marquardt within IRLS (LM-IRLS) routine. For  $N = |\mathcal{V}|$  keyframes, the per-edge residuals, Huber reweights, and analytic Jacobians of Sec. A.2 are accumulated in parallel on the GPU into a sparse block Hessian  $H \in \mathbb{R}^{7N \times 7N}$  and gradient  $g \in \mathbb{R}^{7N}$ . Partitioned per-keyframe tangent vectors  $\tau_i \in \text{sim}(3)$  then satisfy the damped normal equations

$$\left( H + \lambda \text{diag}(H) + \epsilon_r \mathbf{I} \right) \tau = -g, \quad T_{WC_i} \leftarrow \text{Exp}(\tau_i) T_{WC_i}, \quad (25)$$

with  $\lambda$  the LM damping coefficient and  $\epsilon_r$  a Tikhonov regulariser, and the left-perturbation retraction of Sec. 3.2. The local-per-agent and global bundle-adjustment paths run inside a CUDA backend that pins  $\lambda \equiv 0$  at all call sites and uses a Tikhonov-only escalation starting at  $\epsilon_0 = 10^{-6}$ , so Eq. (25) reduces to a Tikhonov-regularised Gauss-Newton step in those two solvers. The pose of the single anchor keyframe at global index 0 is held fixed to remove the global Sim(3) gauge freedom, and only the remaining  $N - 1$  poses are updated.

**Huber-IRLS reweighting.** The robust outer loop is a standard iteratively reweighted least squares. At every LM iteration, each residual contributes to  $H$  and  $g$  a multiplicative weight  $w(r) = \min(1, k/|r|)$  with the Huber breakpoint  $k = 1.345$ , recomputed from the residuals of the previous iterate. This is the same robust kernel used inside the tracking energy of Eq. (2), and it produces a smooth bounded influence function that down-weights residuals incurred by outliers without discarding them outright.

**Sparse Cholesky and Tikhonov escalation.** The damped system in Eq. (25) is solved by a simplicial sparse Cholesky factorisation of the assembled  $7N \times 7N$  Hessian. Multi-agent loop-closure graphs frequently produce ill-conditioned Hessians for which a plain factorisation fails; we therefore escalate the Tikhonov term geometrically,  $\epsilon_r = \epsilon_0 \cdot 100^r$  with  $\epsilon_0 = 10^{-6}$ , for up to  $R = 6$  retries ( $\epsilon \in \{10^{-6}, 10^{-4}, 10^{-2}, 10^0, 10^2, 10^4\}$ ) until the factorisation succeeds. This regularisation is a numerical safeguard only; on a well-conditioned system the very first attempt ( $r = 0$ ) is used and the step is a near-pure Gauss-Newton update. If all six attempts fail, and the solver returns a zero step.

**Convergence criterion.** The per-frame tracker, which evaluates the joint cost each outer iteration, terminates when either the relative cost decrease falls below  $10^{-3}$  or the global step norm  $\|\tau\|_2$  falls below  $10^{-3}$ . The per-agent local solve and the global bundle adjustment skip the cost evaluation and terminate solely on the step-norm criterion  $\|\tau\|_2 < 10^{-8}$ . The per-frame tracker uses up to 50 outer iterations; the per-agent local solve uses up to 10; the in-stream global solve uses up to 50; the terminal cleanup passes use up to 100 each, as detailed in the alternation schedule of Sec. A.7.

## B.3 Cross-Agent Retrieval Backend

The cross-agent retrieval step of Sec. 3.4 is built directly on top of the MAST3R retrieval head. Concretely, each keyframe’s MAST3R encoder tokens are passed through the HOW-style projection branch of [53]. That branch chains an input pre-whitening, a low-rank projector, a per-token attention map, and an output post-whitening, and emits one  $\ell_2$ -whitened local descriptor and one attention score per spatial token. The top- $N_{\text{loc}}$  tokens by attention are kept as the keyframe’s local descriptors. The descriptors are aggregated by binary ASMK [54]. The resulting per-keyframe ASMK record is appended to a single shared inverted-file (IVF) database that is owned by the coordinator and tagged by agent identity; nearest-centroid search inside the IVF runs on a Faiss  $L_2$  index. For each new keyframe we issue one query against this shared IVF, keep only the top  $k_{\text{NN}} = 3$  retrieved keyframes that belong to a different agent than the query, and reject any candidate whose ASMK similarity falls below the threshold  $5 \times 10^{-3}$  of Table 3; survivors enter the dense geometric-verification stage of Sec. 3.4. The hyperparameter values are reported in Table 3.

## B.4 Datasets and Per-Agent Stream Construction

We evaluate on two outdoor benchmarks. **Tanks and Temples (T&T)** [1] contributes four outdoor scenes; **Waymo Open** [59] contributes four driving sequences. For each sequence, we manually pre-split the original monocular RGB stream into two small-overlapping sub-sequences and stage them as two separate frame directories, simulating a pair of robots traversing the same scene independently and meeting only at the trajectory’s overlap regions; the two directories are then handed to the system at launch as the input streams of the two agents, one directory per agent. Images are resized so that the longer side is 512 pixels before being fed to the MAST3R prior; in the calibrated regime, the per-sequence intrinsic matrix is rescaled to the same resolution and the principal point is recentred so the calibrated rays of Eq. (16) stay consistent across resolutions.

## B.5 Evaluation Protocol and Metrics

Tracking accuracy is reported as the Absolute Trajectory Error (ATE) RMSE in metres, computed per agent with the standard EVO evaluation toolkit, which aligns the estimated trajectory to ground truth with a closed-form Sim(3) Umeyama alignment. We deliberately align in Sim(3) rather than SE(3) because our front-end and back-end optimize on Sim(3) throughout: any residual gauge or scale drift inherited from the monocular prior is absorbed into the alignment. Per-scene results in Tables 1, 2, and 6 are the means of the two per-agent ATE values for the scene.

For reconstruction, each keyframe’s globally-optimized canonical pointmap is thresholded by MAST3R confidence ( $C > C_{\text{conf}}$ ), coloured from the original RGB frame, and concatenated across all keyframes of all agents into a single fused, coloured point cloud.

## B.6 Hyperparameters

Table 3 lists every hyperparameter used in the reported experiments, grouped by subsystem. All values match the released configuration; the only ablation knob we vary between Tables 1-2 and Table 6 is the boolean known-calibration switch, which substitutes the residual of Eq. (6) with that of Eq. (17).

# C Additional Experimental Results

## C.1 Ablation Studies

This subsection isolates the contribution of two design choices that the main paper folds into the headline configuration: the cross-agent loop closure that fires inside the global Sim(3) bundle adjustment of Eq. (5), and the per-segment log-scale parameterisation of the terminal depth refinement of Eqs. (19)-(23). All numbers are produced in the uncalibrated regime, so they are directly comparable to the headline T&T column of Table 1, and follow the same per-agent ATE RMSE [m] protocol of Sec. B.5.

**Loop closure.** Table 4 reports per-agent and per-scene ATE on the four T&T sequences with and without cross-agent loop closure, while keeping every other component of the system unchanged. With loop closure, the average ATE drops from 0.099 m to 0.051 m on Barn and from 0.091 m to 0.053 m on Truck, a relative improvement of 48.5% and 41.8% respectively. The mechanism is the one detailed in Sec. A.3-Sec. A.4: once two agents have been geometrically verified, the closed-form Umeyama gauge synchronisation of Eq. (14) transports the moving chain into the anchor’s gauge with a metric-consistent scale, and the subsequent global Sim(3) solve redistributes the cross-agent residual through both agents’ trajectories rather than letting it accumulate at the meeting point. The Ignatius sequence is the one case where the average ATE is slightly worse with loop closure (0.144 m vs. 0.115 m); inspecting the per-agent breakdown, this is driven by a single agent’s chain (0.218 m), where the locally-symmetric statue surface yields a small number of borderline-confidence cross-agent matches that survive the verification gate of  $\tau_{\text{inter}}=0.1$  and pull the gauge in a direction that the per-agent retrieval cannot self-correct, so the gauge-aligned solve trades a

Table 3: Hyperparameter settings used throughout the paper.

Subsystem	Symbol	Value	Meaning
Front-end input	$H \times W$	512 (long side)	MASt3R input resolution
Front-end input	-	30 Hz	Nominal frame rate
Front-end input	-	subsample 2	Multi-agent frame stride
Tracking (Eq. (2))	$\sigma_r$	$3 \times 10^{-3}$	Unit-ray noise
Tracking (Eq. (2))	$\sigma_d$	10	Range noise
Tracking, calibrated (Eq. (17))	$\sigma_p$	1	Pixel-reprojection noise
Tracking, calibrated (Eq. (17))	$\sigma_z$	10	Log-depth noise
Tracking (Eq. (2))	$k$	1.345	Huber breakpoint
Tracking (Eq. (2))	-	$50 / 10^{-3} / 10^{-3}$	max iters / rel-cost tol / step tol
Keyframing	-	0.333	$\min(\nu, \nu_{\text{uniq}})$ threshold for new KF
Keyframing	$Q_{\text{min}}$	1.5	Min descriptor confidence
LM solver, tracker (Eq. (25))	$\lambda_0$	$10^{-6}$	Initial LM damping (tracker only)
LM solver, tracker (Eq. (25))	$\lambda_{\text{max}}$	$10^3$	Max LM damping (tracker only)
LM solver, tracker (Eq. (25))	$\epsilon_r^{\text{min}}$	$10^{-9}$	Tikhonov floor (tracker only)
LM solver, local/global (Eq. (25))	$\lambda$	0	LM damping pinned to zero in CUDA backend
LM solver, local/global (Eq. (25))	$\epsilon_0$	$10^{-6}$	Tikhonov base (CUDA backend)
LM solver, local/global (Eq. (25))	$R$	6 (up to $\epsilon = 10^4$ )	Tikhonov retries on Cholesky failure
Local per-agent solve	-	10 iters, pin 1	Max iters; # fixed keyframes
Local per-agent solve	-	$10^{-8}$	Step-norm tolerance $\ \tau\ _2$
Cross-agent retrieval	-	64k	ASMK codebook size (released, frozen)
Cross-agent retrieval	-	binary, no IDF, $\alpha=3$	ASMK kernel / weighting / selectivity
Cross-agent retrieval	-	1 / 5	Multiple assignment (build / query)
Cross-agent retrieval	$k_{\text{NN}}$	3	ASMK top- $k$ per query
Cross-agent retrieval	-	$5 \times 10^{-3}$	ASMK similarity threshold
Inter-agent verification	$\tau_{\text{inter}}$	0.1	Min cross-agent match fraction
Gauge sync (Eq. (14))	$N_c^{\text{min}}$	64	Min correspondences for Umeyama
Global BA	-	1 edge	Trigger interval
Global BA (in-stream)	-	50 iters	Max LM-IRLS iterations
Global BA (cleanup)	-	100 iters $\times$ 5 passes	Max iters / max passes
Global BA (cleanup)	-	5 mm	Early-stop max $\ \Delta t\ $
Depth refinement (Eq. (19))	$M_k$	$\approx 200$	SLIC target seed count per KF
Depth refinement (SLIC)	-	compactness 8.0, $\sigma = 1.0$	SLIC trade-off and pre-blur
Depth refinement (SLIC)	$C_{\text{min}}^{\text{SLIC}}$	1.5	Pixel-mask confidence threshold
Depth refinement (Eq. (21))	$\sigma_{\text{point}}$	0.05	Point measurement noise
Depth refinement (Eq. (20))	$\lambda_{\text{smooth}}$	1.0	Boundary weight
Depth refinement (Eq. (20))	$\lambda_{\text{prior}}$	1.0	Prior weight
Depth refinement (Eq. (24))	$\lambda_{\text{lm}}$	0.05	Multiplicative LM damping
Depth refinement (Eq. (24))	$s_{\text{max}}$	0.5	Per-iter $ \Delta s_g $ clip
Depth refinement	-	10 inner iters	Per-call segment Newton iterations
Alternation (Sec. A.7)	$R$	100	Max alternation rounds
Mesh visualisation	$\tau_{\text{slant}}$	0.1	Grazing-angle cull in viewer geometry shader
Mesh visualisation	$C_{\text{conf}}^{\text{viz}}$	GUI slider	Per-pixel confidence threshold for quad emission

Table 4: Ablation of cross-agent loop closure on Tanks and Temples [1]. ATE RMSE [m] is reported per agent and as the per-scene average, with all other components (front-end, gauge synchronisation, depth refinement) held fixed. The “w/ Loop Closure” columns reproduce the default configuration; “w/o Loop Closure” disables the cross-agent retrieval and verification of Eq. (12).

Scene	w/ Loop Closure			w/o Loop Closure			Scene	w/ Loop Closure			w/o Loop Closure		
	Agent 1	Agent 2	Average	Agent 1	Agent 2	Average		Agent 1	Agent 2	Average	Agent 1	Agent 2	Average
Barn	<b>0.057</b>	<b>0.045</b>	<b>0.051</b>	0.094	0.103	0.099	Ignatius	<b>0.070</b>	0.218	0.144	0.131	<b>0.098</b>	<b>0.115</b>
Caterpillar	<b>0.092</b>	<b>0.112</b>	<b>0.102</b>	0.097	0.124	0.111	Truck	<b>0.060</b>	<b>0.046</b>	<b>0.053</b>	0.096	0.086	0.091

small amount of accuracy on the noisier agent against a tighter inter-agent constraint. Loop closure remains a net positive on the dataset average and is the default in all reported numbers.

**Depth parameterisation.** Table 5 compares three variants of the alternating depth-pose refinement of Sec. A.7 on Barn and Truck scenes, with the rest of the pipeline held fixed. The **per-pixel** variant exposes one log-scale per pixel and drops the segment boundary term, so the data residual of Eq. (21) drives every pixel independently with only the per-pixel prior of Eq. (23) acting as regulariser. The **per-pixel + Laplacian** variant adds a 4-neighbourhood Laplacian smoothness penalty on log-depth, which is the natural per-pixel analogue of the segment boundary term of Eq. (22) but lives in the full pixel-resolution unknown space. The **per-segment (SLIC)** variant is the configuration of Sec. A.6, in which SLIC on per-pixel normals and log-range groups each keyframe into roughly 200 compact segments and the per-segment boundary term of Eq. (22) couples adjacent log-scales. On

Table 5: Ablation of the depth parameterisation used inside the alternating pose-depth refinement of Sec. A.7 on Tanks and Temples [1] with ATE RMSE [m]. “Per-pixel” exposes one log-scale per pixel with only the prior of Eq. (23); “Per-pixel + Laplacian” adds a 4-neighbourhood log-depth Laplacian smoothness penalty; “Per-segment (SLIC)” is the configuration of Sec. A.6, in which SLIC on geometry channels groups each keyframe into compact segments coupled by the boundary term of Eq. (22). All other components are held fixed.

Scene	Per-pixel			Per-pixel + Laplacian			Per-segment (SLIC)		
	Agent 1	Agent 2	Average	Agent 1	Agent 2	Average	Agent 1	Agent 2	Average
Barn	0.086	0.051	0.068	0.085	0.054	0.070	<b>0.057</b>	<b>0.045</b>	<b>0.051</b>
Truck	0.069	0.052	0.061	0.064	0.051	0.058	<b>0.060</b>	<b>0.046</b>	<b>0.053</b>

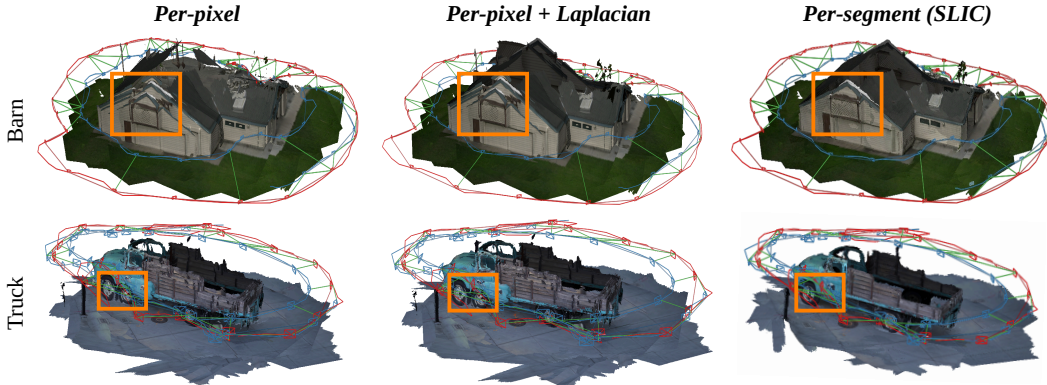


Figure 6: Qualitative comparison of the three depth parameterisations of Table 5 on the Barn and Truck scenes. **Per-segment (SLIC)**: geometry-aware segments cut the parameter count from  $H \times W$  to  $\sim M_k$  per keyframe, so the joint pose-depth alternation of Sec. A.7 stays well-conditioned and recovers crisper boundaries that follow the underlying MAST3R prior.

Barn, the per-segment parameterisation reduces ATE from 0.068 m (per-pixel) and 0.070 m (per-pixel + Laplacian) to 0.051 m. Two effects combine to produce this gap: the SLIC segments cut the depth degrees of freedom by two to three orders of magnitude (from  $H \times W$  pixels per keyframe to  $M_k \approx 200$  scalars), so the joint pose-depth alternation of Sec. A.7 stays well-conditioned even when the cross-agent data term is sparse, and grouping by surface-normal and log-range respects 3D discontinuities, so the boundary residual penalises only depth jumps that the prior itself does not predict. Figure 6 visualises the three depth refinement variants on a Barn and Truck scenes: the per-pixel and per-pixel + Laplacian reconstructions are noisier on weakly-textured regions and ragged along silhouette boundaries, while the per-segment refinement recovers crisp ground-plane and façade structure that aligns with the underlying MAST3R prior without the per-pixel speckle.

## C.2 Known vs. Unknown Calibration

The headline numbers of Tables 1 and 2 are produced in the uncalibrated regime, where every residual, association, and optimisation operates purely on the rays and ranges predicted by the learned MAST3R prior (Eq. (6)). This subsection isolates the contribution of the known-calibration switch of Sec. A.5, which is the only boolean we toggle between the two modes, leaving the front-end, the cross-agent association, the gauge synchronisation, and the depth refinement otherwise untouched. When calibration is enabled, each canonical pointmap is locked to the  $K$ -rays via Eq. (16) before it enters tracking, the global Sim(3) bundle adjustment, or the depth refinement, and the per-match residual of Eq. (6) is replaced with the pixel-reprojection plus log-depth residual of Eq. (17).

Table 6 reports the resulting per-scene ATE on the four T&T sequences. On the dataset average, calibration tightens ATE from 0.094 m to 0.044 m, more than a  $2\times$  improvement, and the gain is consistent across scenes: 0.051  $\rightarrow$  0.043 m on Barn, 0.102  $\rightarrow$  0.089 m on Caterpillar, 0.144  $\rightarrow$  0.021 m on Ignatius, and 0.053  $\rightarrow$  0.023 m on Truck. The takeaway is that CoMo3R-SLAM remains the best-in-class uncalibrated multi-agent system on these benchmarks (Table 1), and that the same system can additionally consume calibration when it is available, reaching accuracy that we are not aware of being matched by any prior monocular collaborative SLAM at this trajectory length.

Table 6: Quantitative comparison of tracking accuracy (ATE RMSE [m]) across different modes of CoMo3R-SLAM and scenes on the Tanks and Temples dataset [1]. <sup>§</sup> indicates our system with known calibration: each pointmap is constrained to the calibrated ray bundle via Eq. (16) and the per-match residual is replaced by the pixel-reprojection plus log-depth residual of Eq. (17). <sup>‡</sup> indicates the default uncalibrated regime of Eq. (6), identical to the configuration that produces the headline numbers of Table 1.

Method	Input	Barn	Caterpillar	Ignatius	Truck	Avg.
<sup>§</sup> CoMo3R-SLAM (Ours)	RGB	<b>0.043</b>	<b>0.089</b>	<b>0.021</b>	<b>0.023</b>	<b>0.044</b>
<sup>‡</sup> CoMo3R-SLAM (Ours)	RGB	0.051	0.102	0.144	0.053	0.094

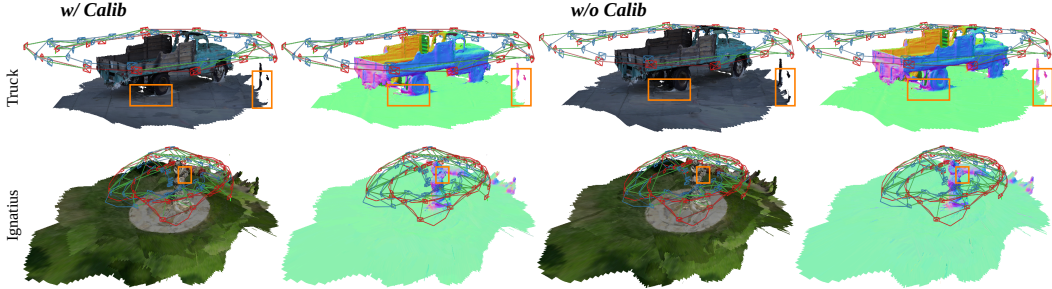


Figure 7: Qualitative comparison of the calibrated and uncalibrated variants of CoMo3R-SLAM on the same Tanks and Temples [1] run. Both variants share a single SLAM pipeline; the only difference is the boolean switch of Sec. A.5 that locks the canonical pointmap to the calibrated ray bundle (Eq. (16)) and substitutes the pixel-reprojection plus log-depth residual of Eq. (17) for the ray-and-range residual of Eq. (6). Calibration sharpens the recovered complex structure and the silhouette of the object.

### C.3 Day-Night Robustness on In-the-Wild Handheld Captures

A practical outdoor multi-agent SLAM system must also operate after dark, where exposure noise, sparse active light sources, and the collapse of low-frequency texture all degrade the appearance signal that a feature-based front-end would normally rely on. This subsection demonstrates that CoMo3R-SLAM is robust across the full illumination range by running the system, end-to-end, on two in-the-wild iPhone captures: a daytime two-agent traversal of one street and a separate night-time two-agent traversal of a second street, each acquired in the wild without any preparation.

**Capture protocol.** We collected two independent two-agent sequences with a handheld iPhone. For the daytime experiment, the same street was walked twice under natural daylight; the two recordings serve as the two agent streams of a single multi-agent run. For the night-time experiment, the same protocol was repeated on a different street after dark, when the only illumination came from street-lamps and ambient light. Each pair of recordings is fed to CoMo3R-SLAM through the launcher used everywhere else in the paper, with no per-sequence tuning and with identical hyperparameters across the two regimes. The iPhone intrinsics are not provided to either run: both experiments execute in the uncalibrated regime of Sec. 3.2, where every residual is the ray-and-range form of Eq. (6) and no  $K$ -matrix ever enters the optimisation.

**Why the system is expected to cope.** CoMo3R-SLAM is well-suited to this regime by construction. The cross-agent association of Sec. A.3 retrieves candidates by ASMK over MAST3R descriptors that were trained on broad outdoor distributions, and the verification gate of Sec. A.4 accepts a candidate only when the geometrically-consistent match fraction  $\tau_{\text{inter}}=0.1$  is reached in both directions, so a candidate must survive a structural test before it can ever affect a pose. The per-match confidence  $q_{mn}$  of Eq. (7) additionally re-weights every residual by the geometric mean of the two endpoint descriptor confidences, so matches whose endpoint is uncertain, which is the regime that dominates at night, are automatically attenuated in both the global Sim(3) solve and the depth refinement without ever needing a lighting-specific heuristic. Once an inter-agent edge passes verification, the closed-form Umeyama synchronisation of Eq. (14) is purely geometric and does not depend on the photometric appearance of the matched pixels, so the gauge transfer behaves identically whether the two agents observe a bright daytime façade or a streetlamp-lit night-time scene.

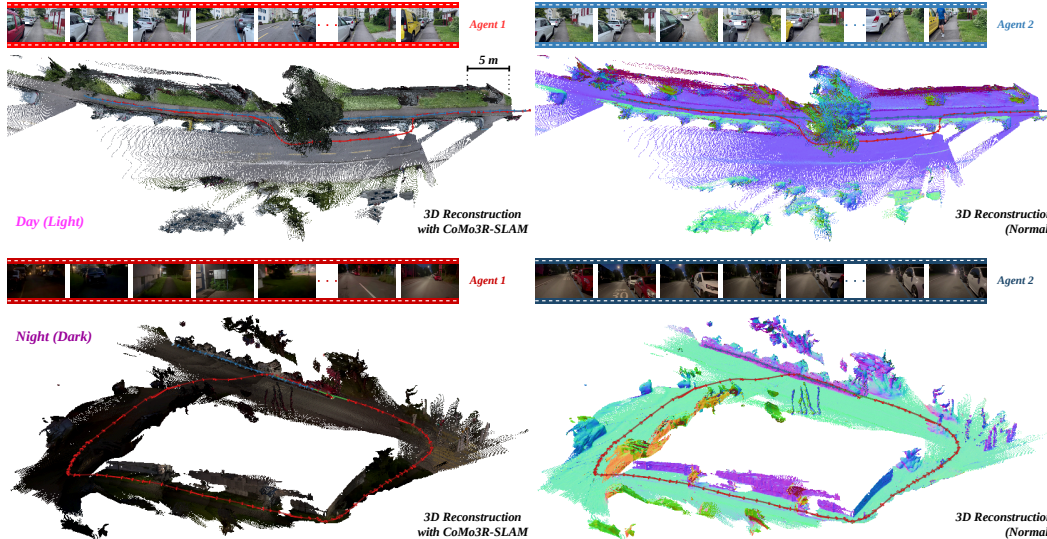


Figure 8: All-time robustness on in-the-wild handheld iPhone captures. We run CoMo3R-SLAM as two independent agents on two separate streets, each traversed twice with a handheld iPhone. Top: the daytime street, where both agents are recorded under natural illumination. Bottom: the night-time street, where both agents are recorded after dark with only streetlamps and ambient light. No camera calibration is supplied to either agent; both runs use the uncalibrated regime of Eq. (6) with identical hyperparameters. The same pipeline that succeeds in daylight also closes the loop between the two night-time agents, demonstrating that the system operates across the full day-night illumination range.

**Result.** Figure 8 shows the two iPhone experiments side by side. In the daytime experiment (top), the two agents recorded along the same street are tied together by verified inter-agent edges and carried into a common metric frame by the global solve, producing a clean fused reconstruction of the façade and ground plane. In the night-time experiment (bottom), the same pipeline closes the loop between the two agents on a different street despite the sparser, lower-contrast appearance signal; the streetlamp- and headlight-lit foreground is recovered consistently across both agents. Critically, neither run receives any camera calibration or any lighting-specific tuning, to handheld iPhone footage captured both at noon and after dark. Together, the two captures demonstrate that CoMo3R-SLAM is robust across the full day-night illumination range in unprepared environments.

#### C.4 Scalability to Three and Four Agents

The main paper evaluates CoMo3R-SLAM in the two-agent regime to match every available multi-agent baseline at the same agent count. The system itself, however, is structurally agnostic to the number of agents: every component, where the per-agent front-end of Sec. 3.3, the union-find component tracker of Sec. A.4, the unified factor graph of Sec. A.3, the global Sim(3) bundle adjustment of Eq. (5), and the segment-level depth refinement of Sec. A.6, which is defined on the flat global keyframe index space  $\{0, 1, \dots, N-1\}$  rather than on a fixed agent count, and the implementation spawns one process per agent and one coordinator with no per-agent specialisation. This subsection verifies that the same pipeline scales transparently to three and four agents.

**Per-agent stream construction.** For each Tanks and Temples scene [1], we partition the original monocular RGB stream into  $N \in \{3, 4\}$  small-overlapping sub-sequences using the same overlap-at-the-meeting-points protocol of Sec. B.4: every adjacent pair of sub-sequences retains a short shared traversal segment so that the cross-agent retrieval has a chance to fire an inter-agent edge between them. Each sub-sequence becomes one agent’s input directory at launch, so it works with no other change to the pipeline.

**Component formation.** The gauge synchronisation of Sec. A.4 is driven by a union-find component tracker rather than by a static agent-index ordering: every accepted inter-agent edge either merges two existing components or attaches a new agent to an existing one, and only the chain of the

component that is not yet connected to the anchor (i.e., agent 0) is transported into the anchor’s gauge. In the three-agent configuration, the first accepted inter-agent edge merges two agents into a single component, and the next edge that connects this component to the third agent pulls that agent’s entire chain into the same gauge in one Umeyama transport; the same logic extends to four agents, with at most three sequential gauge transports bringing all four chains into a single component. The same rigid-snap fallback of Sec. A.4 guards against the rare case in which the first verified edge between two not-yet-connected components is supported by fewer than  $N_c^{\min}=64$  correspondences, so the multi-agent gauge alignment never depends on a single noisy match. The result is that, throughout the three- and four-agent runs, the global factor graph remains a single connected component once the agents have met, and the global  $\text{Sim}(3)$  solve of Eq. (5) acts on every keyframe of every agent simultaneously.

**Reconstruction.** Figure 9 shows the fused dense reconstruction obtained by CoMo3R-SLAM under the three- and four-agent partitions, with each agent’s keyframes colour-coded by agent identity. The reconstruction is a single coherent geometry: every agent’s pointmap contribution lands in the same metric frame and overlaps cleanly with the other agents’ contributions in the meeting regions. The coordinator’s  $7N \times 7N$  Hessian grows with the total keyframe count, not with the agent count, and the sparse Cholesky path of Sec. B.2 absorbs the additional cross-agent edges at constant per-edge cost.

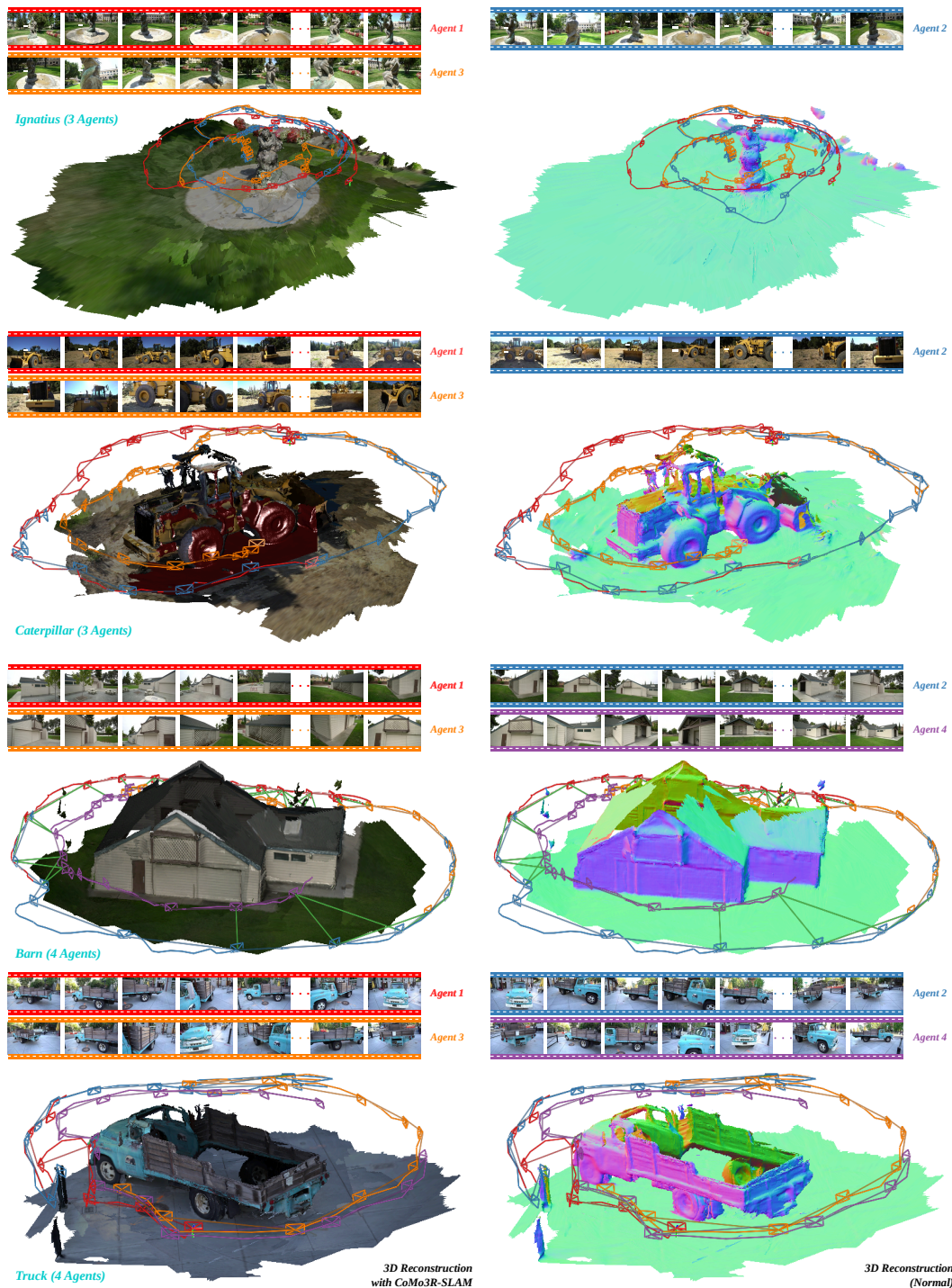


Figure 9: Multi-agent reconstruction with three and four agents on Tanks and Temples [1]. The union-find gauge-transport schedule of Sec. A.4 brings every agent’s chain into a single common  $\text{Sim}(3)$  frame, so the overlap regions between any pair of agents fuse seamlessly without any post-hoc registration step.